scientific reports

Check for updates

OPEN

Revealing seismic sequence characteristics in the south-eastern Alps and the Western Dinarides by clustering analysis and refined location

P. Brondi[1✉], M. Picozzi[1,2], G. De Landro[2], A. G. Iaccarino[2], A. Lomax[3], A. Magrin[1], L. Zampa[1] & M. Michele[4]

The characterization of seismic sequences provides key constraints on fault geometry, rupture processes, and seismic hazard. In this study we investigate seismicity recorded between 2015 and 2024 in the south-eastern Alps and Western Dinarides (SEAWD), one of the most tectonically complex regions of the Alpine–Adriatic domain. Starting from the bulletin seismic catalogue of the Northeastern Italy Seismometer Network, we implement a multiscale relocation workflow. The catalogue is first relocated at regional scale using a multi-iterative NonLinLoc Source-Specific Station Term (NLL-SSST) approach, progressively refining residual grids to account for velocity-model uncertainties. Seismic sequences are then identified through nearest-neighbour clustering. Selected sequences are finally relocated at local scale using waveform-coherence–based NonLinLoc (NLL-coherence), enforcing spatial consistency among similar events. This workflow yields locations with ~hundreds-of-meters resolution and resolves fine-scale fault structures. We identify 71 sequences, mainly foreshock–mainshock–aftershock and mainshock–aftershock types, with limited swarm-like activity. Principal component analysis quantifies sequence volume and orientation of seismicity distributions. Most clusters define tabular structures: larger volumes correspond to planar fault zones, whereas compact clusters involve low-magnitude and low seismic activity. These patterns highlight the structural complexity of the Alpine–Dinaric transition zone and provide new constraints on active seismogenic structures and seismic hazard in northeastern Italy and adjacent regions.

The progressive increase in seismic station density, together with advances in computational capabilities and the development of improved detection and location techniques[1–3], has significantly enhanced our ability to identify seismic sources and to resolve the physical processes governing earthquake occurrence on faults[4]. Consequently, analysis of seismicity has become a key tool for constraining fault geometry and its temporal evolution (e.g., Liu et al.[5], Muzellec[6], Picozzi[7], Picozzi[8], Poggiali[9], Sollai[10], Tan[3]).

The characterization of seismicity patterns is central to seismic hazard assessment, as changes in earthquake occurrence often reflect variations in stress loading and fault interactions. In this context, seismic sequences, defined as earthquakes clustered in space and time relative to background seismicity, provide essential information on fault activation and triggering processes[4,11]. Recent studies have shown that both static stress transfer and fault-zone complexity strongly influence the spatial and temporal evolution of seismic sequences[12–14]. Large cascading events, such as the 2023 Kahramanmaraş sequence in Turkey, illustrate how stress interactions between adjacent fault segments can control earthquake occurrence[15], while swarm-like activity along the Maacama, Northern California fault, highlights the role of small, distributed fault structures in generating complex seismicity[16].

In Italy, seismic sequence analysis has provided important insights into faults structure and rupture processes. The 2016–2017 Central Italy sequence revealed the progressive activation of complex fault systems and clarified the role of fault segmentation and cascading rupture during major earthquakes[3,7,8,17–19]. Other studies

[1]National Institute of Oceanography and Applied Geophysics–OGS, Trieste, Italy. [2]University of Naples "Federico II", Naples, Italy. [3]ALomax Scientific, Mouans-Sartoux, France. [4]Istituto Nazionale di Geofisica e Vulcanologia–INGV, Rome, Italy. ✉email: pbrondi@ogs.it

documented intermittent fault activity, fluid-driven seismic migration, and static stress-controlled sequences in different tectonic settings, including the Altotiberina fault, Molise, and Irpinia[20–24].

The south-eastern Alps and Western Dinarides (SEAWD) constitute a region of high tectonic complexity and moderate-to-high seismic hazard, with the 1976 M_W 6.5 Friuli earthquake marking the most recent destructive event. Subsequent investigations of major sequences, such as the 1998 and 2004 Bovec–Krn earthquakes, revealed complex fault geometries and stress heterogeneities controlled by regional tectonics[25]. Later studies showed that mainshock-induced stress changes can promote progressive damage accumulation and subcritical crack growth, processes enhanced by mechanical contrasts and unclamping effects[26], and highlighted the role of fluid transients bound to strong to moderate earthquakes in the stress field variation and in modulating the background seismicity[27]. More recent analyses in the SEAWD region have emphasized the influence of fault interactions and mechanical heterogeneity on the spatial and temporal distribution of seismicity[28].

In this study, we analyze the seismic sequences that have occurred in the SEAWD region over the past decade using approximately 17,000 seismic events from the National Institute of Oceanography and Applied Geophysics (OGS) high-quality catalogue (Fig. 1a). The selected events have focal depths between 0 and 45 km and were recorded by stations belonging to the OGS[29] and other nearby seismic networks (Fig. 1b; see the "Data" section for more details). Focusing on the period after 2015 ensures an improved hypocentral accuracy in terms of location uncertainties and azimuthal coverage[30]. Based on various geophysical characteristics observed in previous studies, we organize our discussion of results dividing the SEAWD region into three subdomains (Fig. 1b): Western SEAWD (WS), Central SEAWD (CS), and Eastern SEAWD (ES). The WS area experienced over the last decade low seismicity, characterized by swarm activity and structures with subvertical strike-slip (NNE–SSW, N–S) and normal NW–SE focal mechanisms with a southwest dip[4]. The CS area has the highest seismicity in the entire Alpine arc, close to the epicenter of the 1976 M_W 6.5 Friuli earthquake, and is characterized by a predominance of mainshock-aftershock sequences with a mainly thrust faulting regime[4,31]. Finally, the ES area, located in the transition zone between the Alps, the Dinarides, and the Pannonian Basin, is characterized by active faults with a NW–SE orientation, parallel to the Dinarides chain, exhibiting right-lateral strike-slip movement that extends for tens of kilometers and produces both swarms and sequences[32,33].

The outline of our analyses in the SEAWD area is presented in Fig. 2. Starting from the OGS bulletin seismic catalogue and its corresponding 1D velocity model[34], seismicity is first relocated at the regional scale using a multi-scale approach based on NonLinLoc-source-specific station travel-time corrections (NLL-SSST[35]), which progressively refines the time residual grids to mitigate velocity-model uncertainties. On the resulting high-precision catalogue, seismic sequences are identified through nearest-neighbour clustering[36,37] and subsequently relocated to higher precision at the local scale with a waveform-coherence-based NonLinLoc approach (NLL-coherence[35]). Specifically, we will use the term NLL-SC to refer to sequential application of the NLL-SSST and then NLL-coherence methodologies. Our strategy enables a detailed characterization of the spatial and temporal evolution of seismic sequences. Sequences are subsequently classified according to their temporal behavior (e.g., foreshock–mainshock–aftershock, mainshock–aftershock, and swarm-like activity), while their spatial extent is quantitatively characterized through principal component analysis (PCA), used to derive a first-order estimation of sequence volume (Fig. 2). Overall, this approach provides a consistent basis to investigate sequence geometry, rupture processes, and fault-zone structure, with implications for seismic hazard assessment in northeastern Italy and adjacent regions.

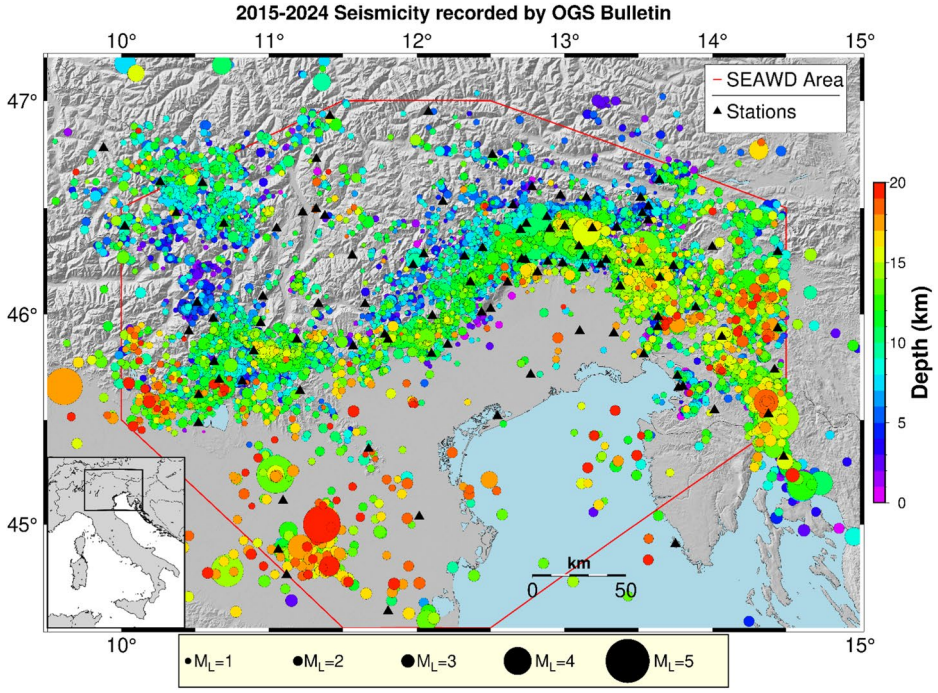
Results

Selection and relocation of the sequences

We applied the NLL-SSST analysis to the OGS bulletin catalogue. Prior to relocation, we assessed the magnitude of completeness Mc of the original catalogue, obtaining Mc = 0.6 using the approaches described by Wiemer et al.[52] and Iaccarino and Picozzi[38] (see Supplementary Figure S1). The NLL-SSST procedure allowed us to relocate 16,053 events (i.e., representing 93% of the original dataset), while the remaining events were discarded due to insufficient quality according to the NLL-SSST location criteria (see "Methods" section and Fig. 3a).

Comparing Figs. 1a and 3a, we see that the most significant difference between the locations of the OGS bulletin and those of NLL-SSST is in hypocentral depth, with the difference Δz between the depth of events relocated by NLL-SSST and the depth of events in the bulletin being predominantly negative in two broad longitudinal sectors, approximately between 10.2°–11.0°E and 11.5°–14.0°E (Fig. 3a). To facilitate the interpretation of this pattern, Fig. 3a also includes labels indicating the sign of $M\Delta z$, where $M\Delta z$ denotes the mean value of Δz within each longitudinal sector. Accordingly, $M\Delta z < 0$ in almost all the WS, CS, and ES areas, except for a narrow intermediate sector (11.0°–11.5°E), where $M\Delta z > 0$. The predominance of negative Δz values indicates that the relocation systematically shifts most hypocentres to shallower depths, while the positive $M\Delta z$ observed in the intermediate sector highlights a localized deviation from this regional trend. This result suggests that in all three areas - WS, CS and ES -, NLL-SSST implies a medium with a higher wavespeeds than that used for the creation of the OGS bulletin. Figure 3 also shows north-south cross sections at longitudes 13.0°E and 13.25°E (CS area) for the OGS bulletin (Fig. 3b and c) and NLL-SSST locations (Fig. 3d and e). For each cross section, earthquakes within a 4 km-wide swath (± 2 km from the section plane) were projected onto the section. By comparing them, we observe that even at this stage of relocation, the structures are geometrically more defined with NLL-SSST than in the initial bulletin data.

In the next step, we separated background seismicity from clustered seismicity in the relocated catalogue using the rescaled generalized distance method by Zaliapin et al.[36]. As a result of the clustering analysis (details are provided in the "Methods" section), 76 seismic sequences, comprising approximately 2,200 events, were identified (Fig. 4; see Supplementary Fig. S2). Looking at the nearest-neighbour proximity parameter $\log(\eta)$ we observe as sequences occur rather regularly distributed in time (Fig. 4a, b), but not in space (Fig. 4c, d). The highest density of sequences is observed in the eastern part of the CS region (Fig. 4c), while apparent gaps



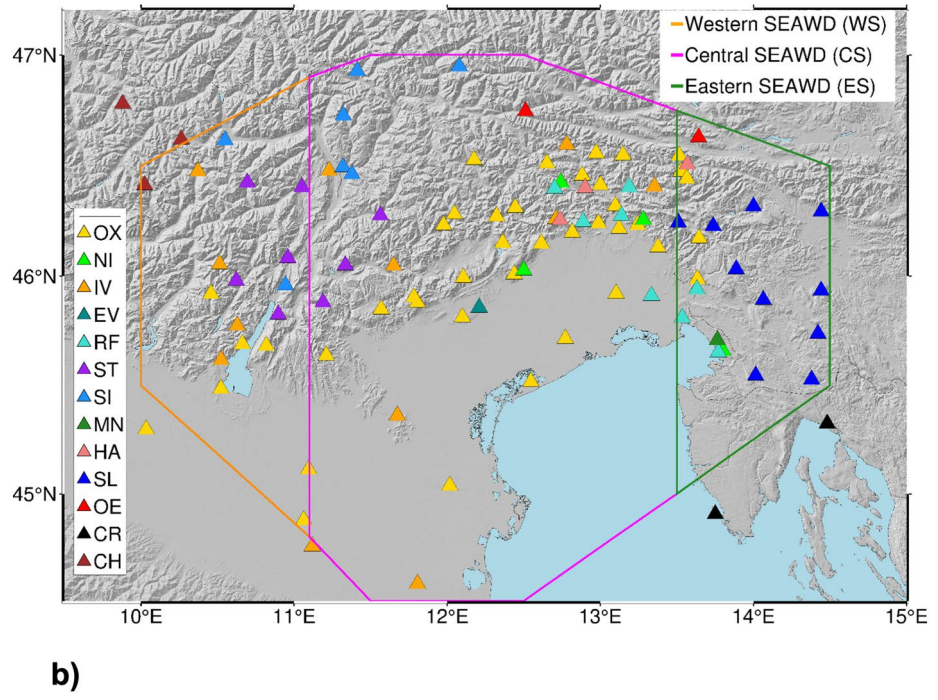


Fig. 1. (**a**) OGS bulletin data in the 0–20 km depth range reported for the SEAWD area; (**b**) subdivision of the SEAWD into three subregions together with the seismic stations used in this study. Stations belong to the OGS (OX), North-East Italy Broadband (NI), Italian National Seismic Network (IV), Collalto (EV), Friuli Venezia Giulia Accelerometric (RF), Trentino (ST), Province Südtirol (SI), MedNet (MN), HAREIA (HA), Austrian (OE), Slovenian (SL), Croatian (CR), and Swiss (CH) seismic networks (see "Data" section for details).

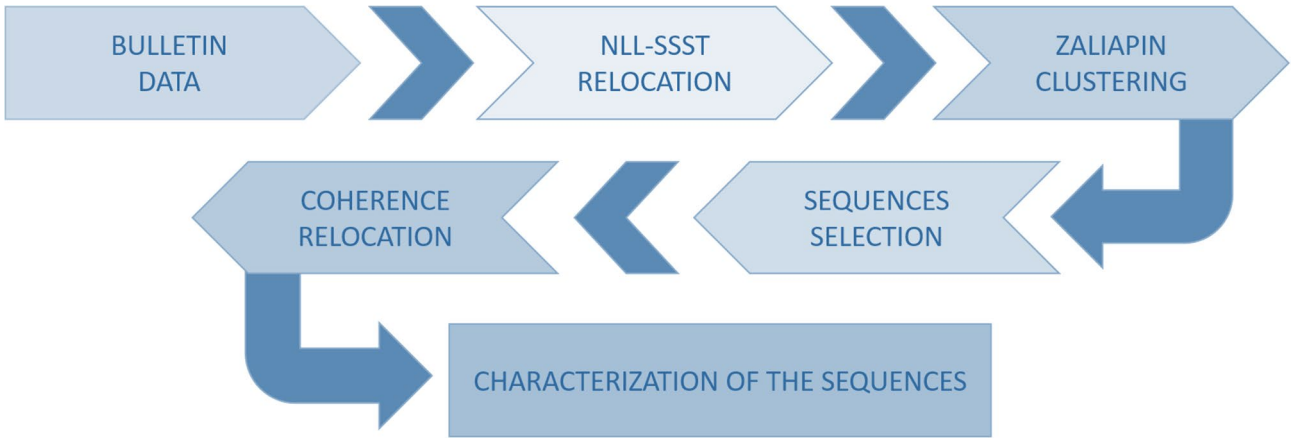


Fig. 2. Flowchart of the analyses for seismic sequences.

between sequences are observed in coincidence with the western part of the CS region (i.e., longitude ~ 12°) and at the junction of the CS and ES areas.

A look at moment magnitude as a function of time (Fig. 4b) does not highlight specific temporal patterns, leading us to exclude, at least in a first approximation, the presence of external forcing driving the sequences occurrence. Clusters concentrate along the main seismogenic belt of the south-eastern Alps, particularly along the southern Alpine thrust front and the Friuli–Slovenia transition zone (FSTZ; indicated in Fig. 3a), while background seismicity (grey) appears more diffusely distributed. Figure 4d presents the depth distribution versus longitude, indicating that most clustered seismicity occurs within the upper crust (≈ 5–15 km depth) and follows the along-strike geometry of the Alpine front. The clustering highlights localized zones of repeated seismic interaction embedded within a broader background seismicity field. The clustering parameters adopted in this study follow previous applications of the nearest-neighbour method[37,39]. Although different parameter choices may slightly modify the number of identified clusters, the main spatial patterns and the concentration of sequences in the Central SEAWD remain stable.

For each indicated sequence, we applied the NLL-coherence stage of NLL-SC (details are provided in the "Methods" section), using waveforms from at least four stations near the median epicentral location to achieve a good balance between signal quality and network coverage. In the following analyses, we consider the maximum-probability hypocentral configuration returned by NLL-SC as the reference estimate of the sequence geometry. This configuration corresponds to the most likely pseudo-relative arrangement of the earthquakes resulting from the coherence-based relocation and therefore constitutes the nominal solution from which all geometrical parameters (PCA, sequence volume) are computed. Due to limited station coverage in the southwestern part of the CS area, the requirement of using waveforms from at least four nearby stations was not met for the M_L 4.4 2023 Ceneselli earthquake sequence (the southernmost sequence in Fig. 4c), resulting in its exclusion from subsequent analyses. Because the seismicity of four sequences in the ES appears to be located near the southeast corner of the SE area, to avoid inaccuracies in characterizing these sequences due to partial event detection, we also excluded them from subsequent analyses. Consequently, our final SEAWD sequence database consists of 71 sequences: 11 within WS, 47 within CS, and 13 within ES. Starting from the absolute location of the OGS bulletin, Fig. 5 shows the effect of the intermediate NLL-SSST relocation procedure and the final NLL-SC relocation procedure for three sequences characterized by some of the strongest mainshock: the M_L 3.8 Ledro sequence (WS) in 2015, the M_L 4.3 Bovec sequence (ES) in 2020, and the M_L 4.6 Socchieve sequence (CS) in 2024. A map showing the locations of these three sequences is provided in Figure S3 of the Supplementary Material. In all three cases, applying NLL-SSST results in more clustered seismicity (Fig. 5b, e,h) than the OGS bulletin data (Fig. 5a, d,g). For the 2015 Ledro and 2024 Socchieve sequences, the events also appear to decrease in depth by a few kilometers. The subsequent application of the NLL-coherence procedure further clusters the seismicity, revealing finer geometric structures (Fig. 5c, f,i).

Specifically, seismicity that, with NLL-SSST, spans 2 km in latitude, 2 km in longitude, and 5 km in depth is subsequently concentrated within 1 km in latitude and longitude and 3 km in depth. Figure S4 in the Supplementary Information shows the root mean square residual (RMS) and the horizontal and vertical errors of the events from the three sequences obtained at the initial iteration of NLL-SSST, the final iteration of NLL-SSST, and the NLL-coherence procedure. In all three cases, the significant reduction in RMS at the last iteration of NLL-SSST compared to the first suggests that the SSST corrections to the initial velocity model allowed better consideration of the medium's heterogeneity, leading to improved location quality (see Supplementary Figures S4a, S4d, S4g). This decrease in RMS results in horizontal and vertical error values that remain the same or are slightly higher than those in the initial iteration (See Supplementary Figures S4b, S4c, S4e, S4f, S4h, S4i). This outcome may be because SSST implicitly introduces a more realistic model, revealing heterogeneities that the initial simple model had previously absorbed. The subsequent application of NLL-SC results in a slight increase in RMS, accompanied by a marked reduction in both horizontal and vertical uncertainties. This behaviour is consistent with the coherence-based relocation strategy, which prioritizes waveform similarity and relative event locations over the minimization of travel-time residuals.

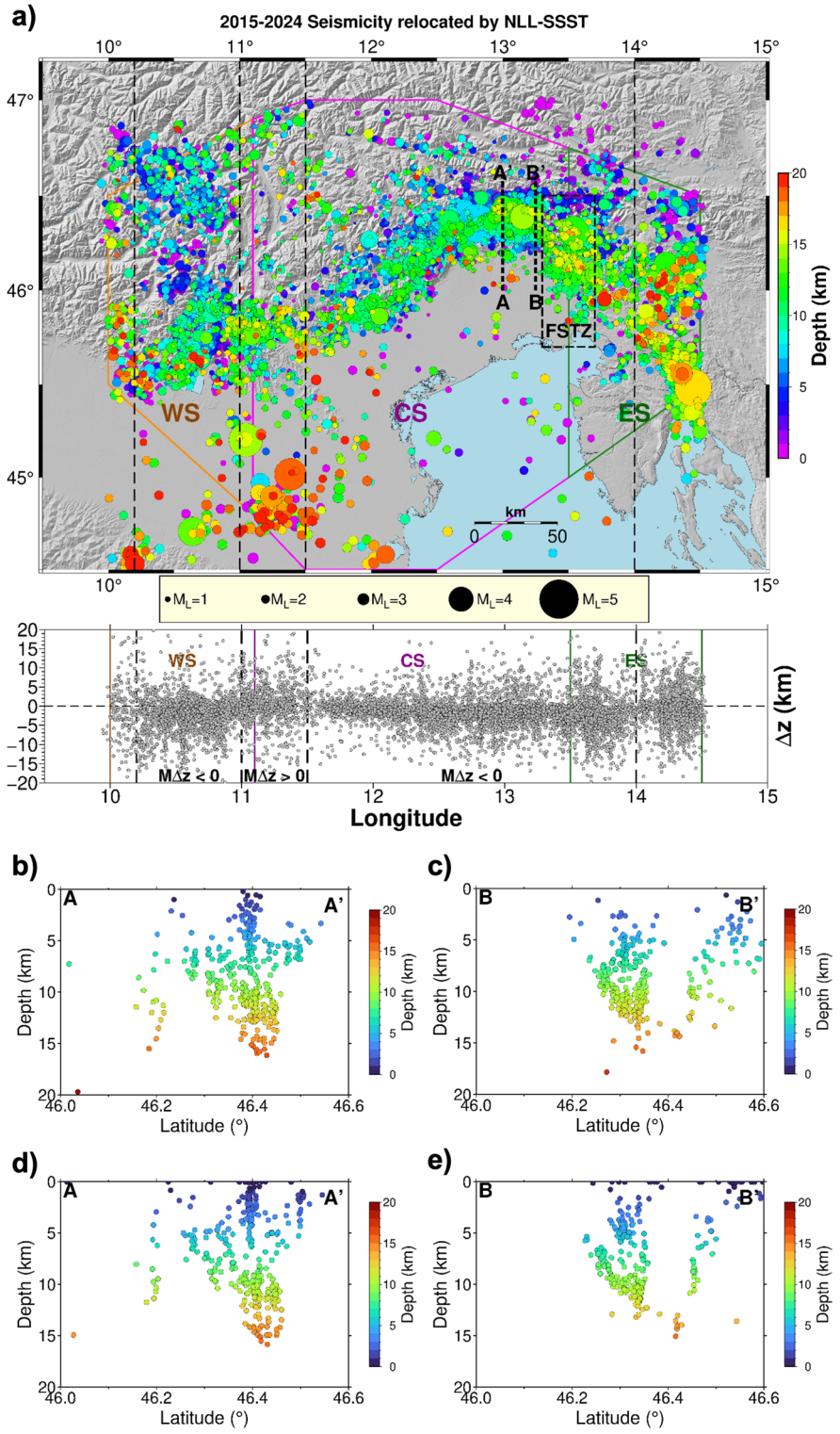


Fig. 3. (**a**) OGS bulletin data relocated by NLL-SSST (top) in the 0–20 km depth range and difference between the depth of the NLL-SSST relocated catalogue and the depth value of the original catalogue Δz (bottom). The vertical black dashed lines delimit longitudinal intervals characterized by different mean Δz (MΔz) values, whereas the colored solid lines mark the boundaries of the Western (WS), Central (CS), and Eastern (ES) SEAWD regions. The black dashed rectangle outlines the approximate extent of the Friuli–Slovenia Transition Zone (FSTZ). (**b**) Cross section of seismicity at longitudes 13.0° and (**c**) 13.25° for the OGS bulletin. (**d**) Cross-section of the seismicity at longitudes 13.0° and (**e**) 13.25° for the relocated catalogue with NLL-SSST.

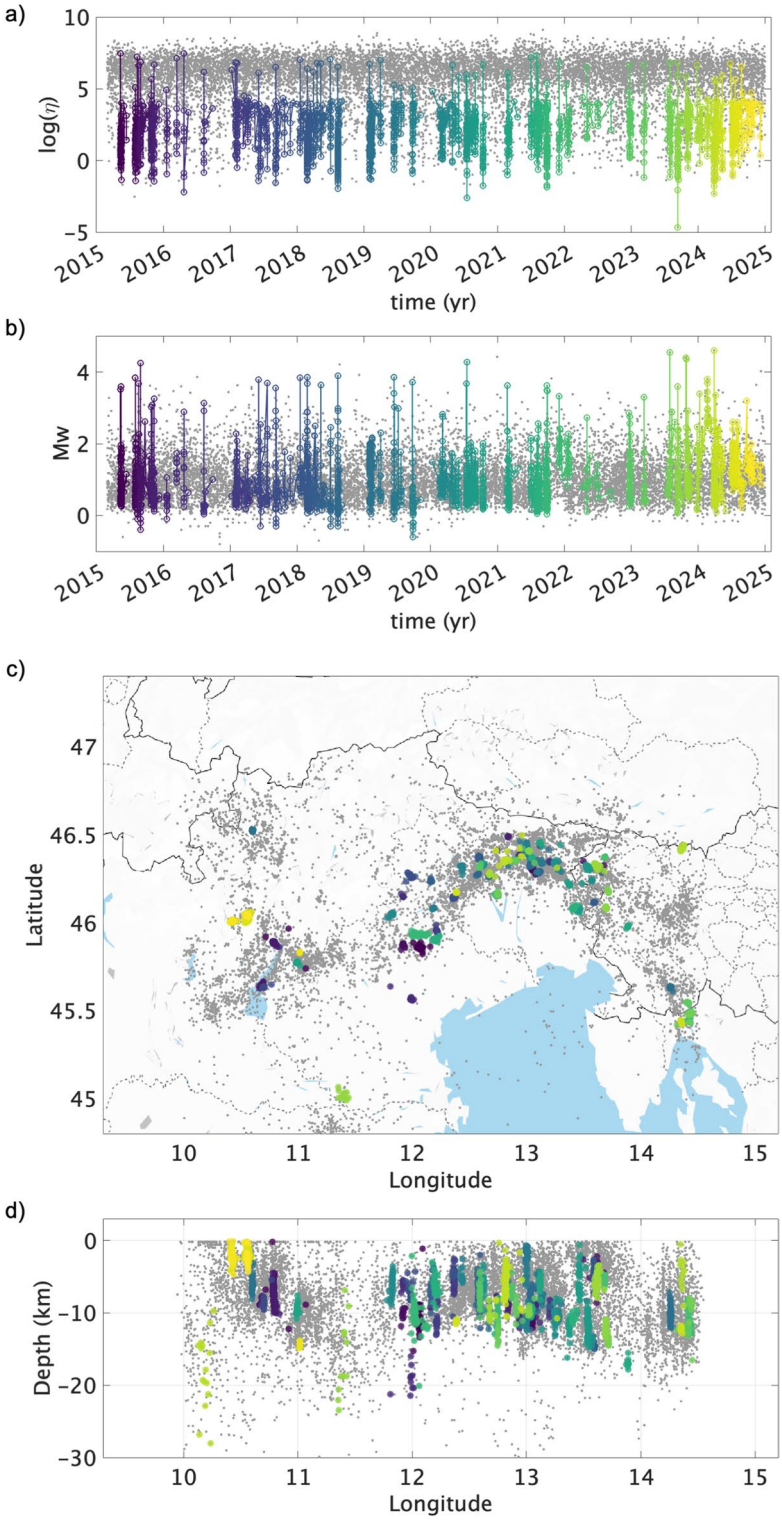


Fig. 4. Sequences identification. (**a**) distribution of log (η) in time for the background seismicity (gray dots) and the identified sequences (dots with the same colour represent a sequence) (**b**) the same as (**a**), but in magnitude. (**c**) Spatial distribution of sequences (background seismicity shown as black dots). (**d**) distribution of background seismicity and seismic sequences for a cross section along longitude.

For the large majority of events of the three sequences, horizontal uncertainties are below 0.5 km and vertical uncertainties below 1 km, although larger vertical uncertainties are observed for some sequences owing to the station geometry and the heterogeneous network coverage across the SEAWD area. These uncertainties represent the absolute location uncertainty estimated by NonLinLoc from the posterior probability density

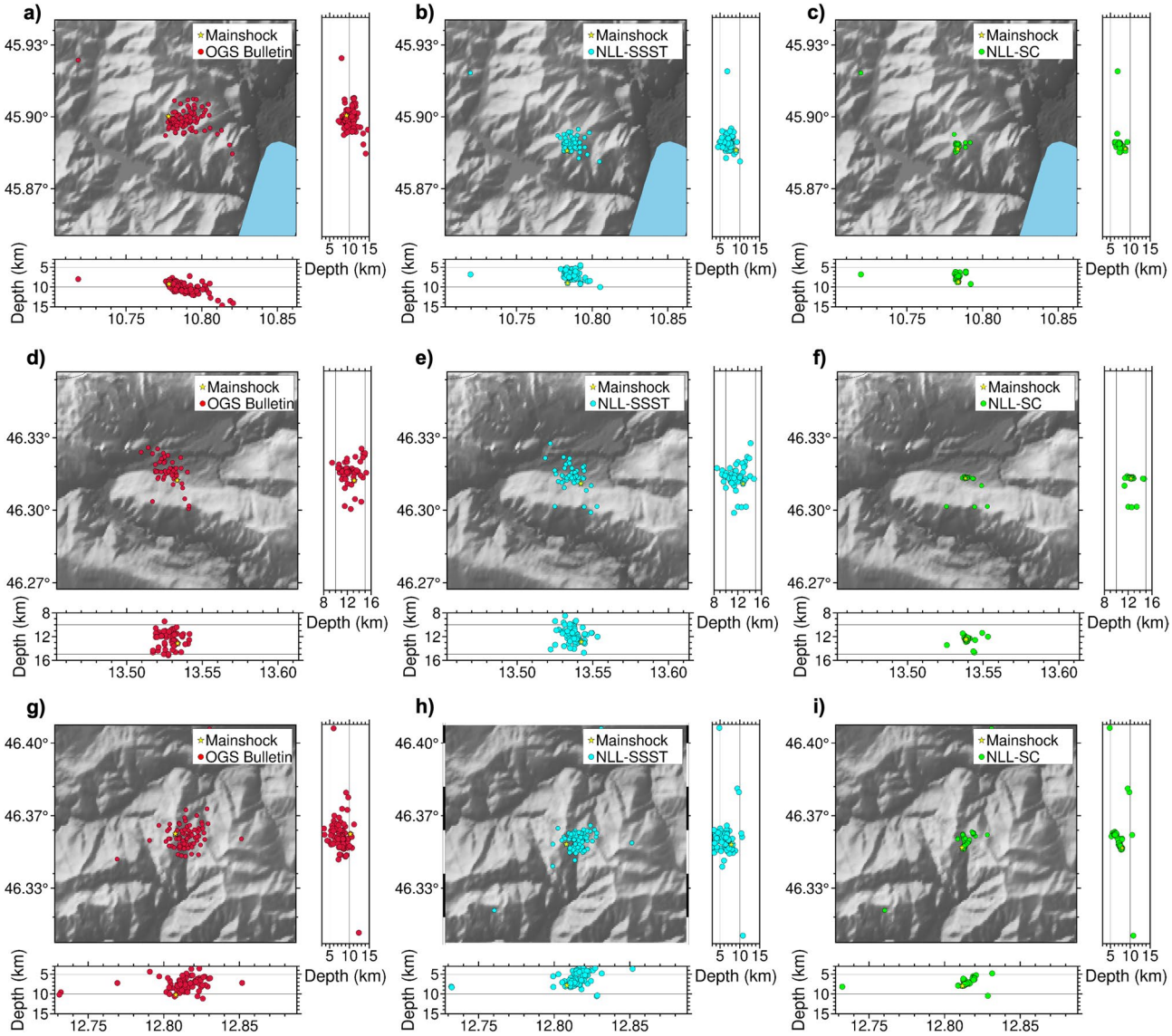


Fig. 5. Example of three sequences' location from OGS bulletin, NLL-SSST and NLL-SC. (**a**–**c**) location for the M_L 3.8 2015 Ledro Sequence. (**d**–**f**) M_L 4.2 2020 Bovec Sequence. (**g**–**i**) M_L 4.6 2024 Socchieve Sequence.

function of each event. As commonly observed in local earthquake locations, vertical uncertainties are generally larger than horizontal ones because of the station geometry and the distribution of seismic stations across the SEAWD region. Although absolute depth uncertainties may locally exceed 1 km, particularly at the edges of the network, the coherence-based relocation primarily improves the relative locations of neighbouring earthquakes by exploiting waveform similarity. Consequently, the relative geometry of each seismic sequence is significantly better constrained than would be inferred from the absolute location uncertainties alone.

To explicitly evaluate the impact of these location uncertainties on the subsequent geometrical analyses, we propagated the complete location covariance matrix of each earthquake through a Monte Carlo uncertainty propagation approach (see "Methods", "Principal component analysis, sequence volume estimation and uncertainty propagation"). The resulting distributions of the Principal Component Analysis (PCA) eigenvalue ratios allowed us to quantify the robustness of the geometrical classification and the uncertainty associated with the estimated sequence volume. Origin-time adjustments introduced by the relocation procedures are typically below 0.5 s, indicating that the inferred temporal evolution of the seismic sequences is essentially unaffected (Figure S5).

Sequences distribution and properties

Figure 6a shows the distribution of the 71 sequences located in the SEAWD area in terms of epicentral position and vertical sections along longitude and latitude. Most of these sequences are found in the CS area (63%), while a significantly lower percentage is found in the WS (15%) and ES (21%). In Fig. 6a the epicentral location of the sequences that occurred in the SEAWD is also compared with surface fault traces from the Database

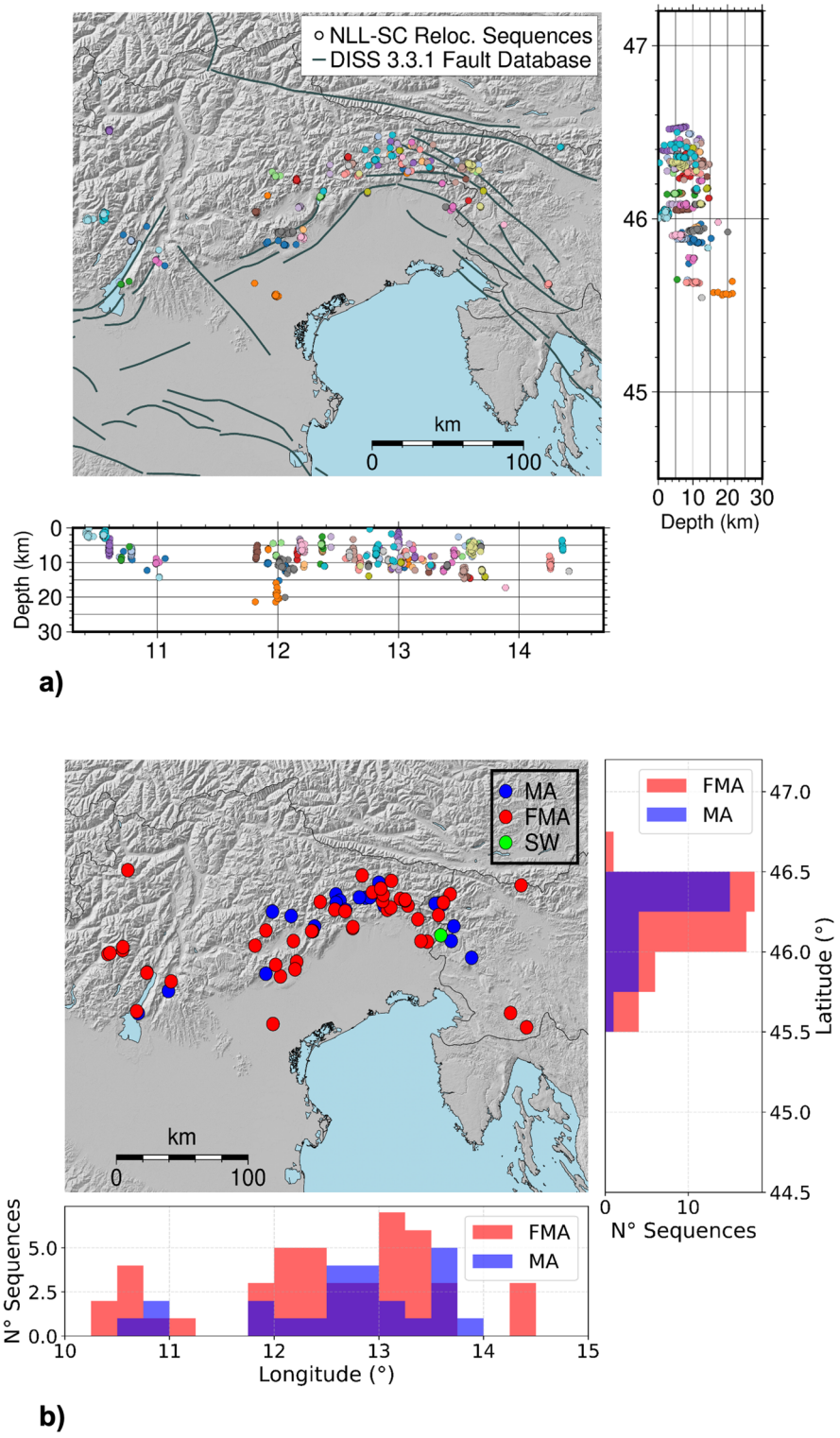


Fig. 6. (**a**) Map view of the 71 seismic sequences relocated with NLL-SC, shown together with the DISS 3.3.1 fault dataset. Each color identifies a different seismic sequence. The accompanying panels show the distribution of the relocated events in map view and in the longitude–depth and latitude–depth cross sections. (**b**) The same 71 relocated sequences grouped by sequence typology: Foreshock–Mainshock–Aftershock (FMA), Mainshock–Aftershock (MA), and Swarm (SW). The accompanying histograms show the number of FMA and MA sequences within each longitude and latitude interval.

of Individual Seismogenic Sources [DISS, version 3.3.1[40]]. Following Ogata and Katsura[41], we classify the seismic sequences on the base of the relative magnitude difference (ΔM) between the mainshock and the largest preceding event: sequences characterized by a dominant mainshock followed by aftershocks were defined as Mainshock–Aftershock (MA) type; sequences including a preparatory phase were classified as foreshock–mainshock–aftershock (FMA) type when ΔM > 0.45; conversely, sequences with ΔM < 0.45, lacking a clearly dominant mainshock, were classified as swarm-type (SW) sequences. We found that 49 sequences are FMA type (65%), 25 are MA type (32%), and 1 is SW type (3%). Supplemental Table 1 in the Supplemental Information presents information on the time, epicenter location, and magnitude of the mainshocks, as well as the type, number of events, and duration of the identified sequences. Interestingly, the FMA sequences are distributed in both the pre-Alpine and Alpine areas of CS, while the Mainshock-Aftershock sequences are mainly found in the CS Alpine area (Fig. 6b). Figure 6b also shows that 60% of MA sequences are located in the latitude range 46°–46.25°, and their number is comparable to that of FMA sequences which are predominant in the longitude range 10°–12.5° (WS and western CS areas), 13°–13.5° (CS area), and 14.25°–14.5° (ES area). Conversely, MA sequences dominate in the central part of the CS area.

Figure 7 shows the sequences for different attributes: duration, magnitude, and depth of the mainshock for the FMA (Fig. 7a–c) and MA (Fig. 7d–f) sequences, respectively. The two types of FMA and MA sequences

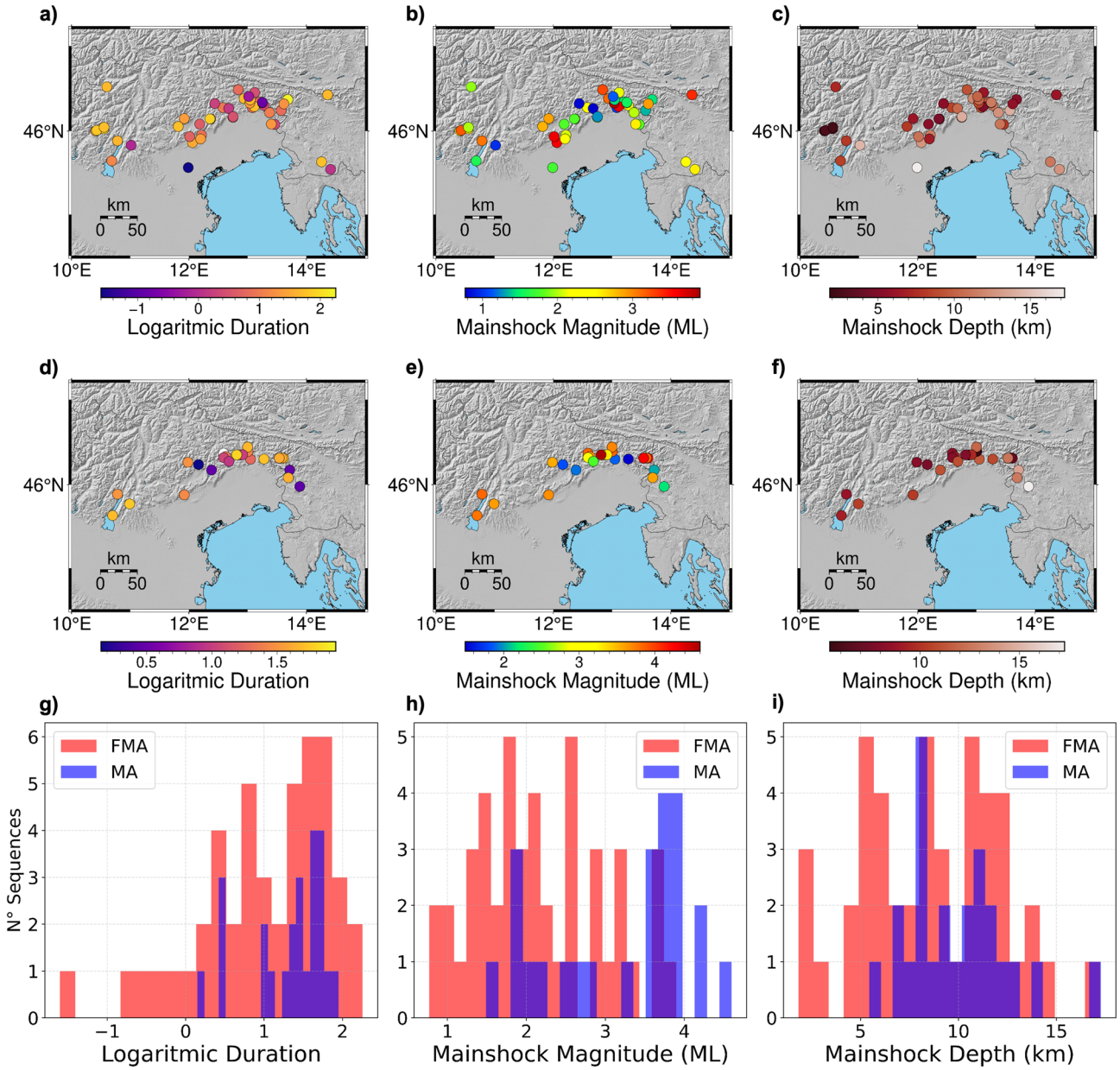


Fig. 7. Logarithm of duration, mainshock magnitude and mainshock depth for the FMA sequences (**a**–**c**) and the MA sequences (**d**–**f**), respectively. Distributions of (**g**) logarithm of duration, (**h**) mainshock magnitude, and (**i**) mainshock depth for the FMA sequences (in red) and the MA sequences (in blue).

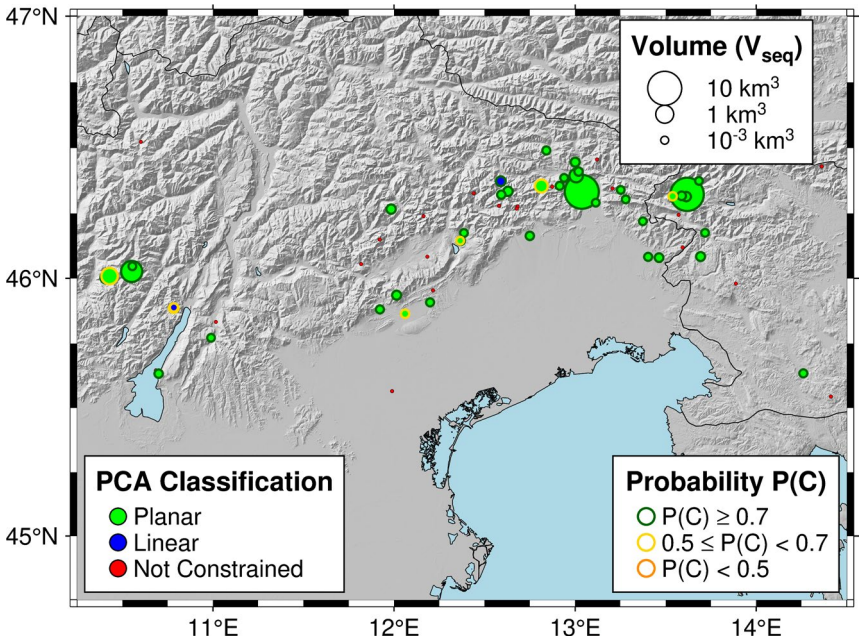


Fig. 8. Volume and geometrical classification of the seismic sequences. The figure shows the spatial extent of each sequence quantified by the seismicity volume (V_{seq}). Colors indicate the geometry of the spatial distribution obtained from the PCA analysis, with sequences classified as planar, linear, or geometrically unconstrained according to the eigenvalue ratios derived from the PCA (see "Methods"). For planar and linear sequences, the maximum classification probability P(C), obtained from the Monte Carlo simulations, is reported, providing a quantitative estimate of the confidence associated with the assigned geometrical class. The values of V_{seq}, the geometrical classification, and the corresponding classification probabilities for each sequence are reported in Supplementary Table 2.

do not appear to differ significantly in cluster duration (Fig. 7g) or mainshock depth (Fig. 7i). Although the three longest sequences are of the FMA type (the February and June 2017 Alpago sequences in the CS area and the 2020 Bovec sequence in ES area; see the Supplementary Table 1), 61% of the 28 sequences lasting more than 30 days are FMA, and 39% are MA. Regarding the mainshock depth, the FMA and MA sequences show almost completely overlapping distributions (Fig. 7i) and lower values in the WS, in the northern part of CS and northwestern part of ES (Fig. 7c–f). The depth of the mainshock in the sequences increases toward the Adriatic Sea and ES area (Fig. 7c–f). Figure 7h shows that, on average, MA sequences have a greater mainshock magnitude than FMA sequences. In particular, the three sequences shown in Fig. 5 (i.e., the 2015 Ledro sequence in WS, the 2020 Bovec sequence in ES, and the 2024 Socchieve sequence in CS; see the Supplementary Table 1) are all of the MA type.

PCA-based characterization of the seismic sequence geometry

The PCA and Monte Carlo procedures described in the "Methods" section were applied to the 71 relocated sequences to estimate their sequence volume (V_{seq}), quantify the associated uncertainties, and characterize their spatial geometry. The Monte Carlo simulations were used to estimate the probability that each sequence belongs to one of three geometrical classes—planar, linear, or geometrically unconstrained—based on the distribution of the realizations in the PCA parameter space (Fig. 8; see "Methods"; Eq. 5). Specifically, the geometrical classification is determined from the ratios between the PCA eigenvalues λ_1, λ_2, λ_3, which describe the relative spatial organization of each sequence (Figure S6; see "Methods"). The maximum class probability, **P(C)**, defined as the highest of the three class probabilities (planar, linear, and geometrically unconstrained) estimated from the Monte Carlo simulations, provides a quantitative measure of the confidence in the geometrical classification (Fig. 8; see Supplementary Table 2). While the final class is assigned according to the highest probability, sequences with low P(C) should be regarded as geometrically ambiguous, as small perturbations of the hypocentral locations frequently lead to alternative PCA classifications.

Figure 8 shows that 56% of the sequences are classified as planar, 41% as geometrically unconstrained, and 3% as linear. The two linear sequences identified are both characterized by an approximately vertical distribution of seismicity. They correspond to the 2015 Ledro sequence in the WS region and the 2018 Forni di Sopra sequence in the CS region (see Supplementary Table 1), with mainshock magnitude (M_{main}) values of M_L 3.8 and M_L 3.9, respectively. Most planar sequences exhibit high classification probabilities (P(C) > 0.8), indicating that the inferred geometry is robust against the hypocentral location uncertainties propagated through the Monte Carlo analysis (see Supplementary Table 2).

The largest V_{seq} values were observed for the 2018 Cavazzo Carnico sequence in the CS (V_{seq} = 6.58 km³), the 2023 Bovec sequence in the ES (V_{seq} = 6.15 km³), and the 2024 Saviore dell'Adamello sequence in the WS (V_{seq} =

1.73 km³). All three sequences are classified as planar and belong to the FMA type (see Supplementary Tables 1 and 2). It should be noted that the V_{seq} values of some sequences located close to the SEAWD boundary may be affected by larger location uncertainties. However, this effect does not appear to be systematic, as sequences with both high and low V_{seq} values occur in these areas (Fig. 8).

Figure S7a suggests a weak first-order positive relationship between $\log(V_{seq})$ and M_{main} for planar and linear sequences, although considerable scatter is observed. The V_{seq} values are shown together with their uncertainties estimated from the Monte Carlo distributions. Despite the width of these uncertainty intervals, they do not alter the overall positive trend between $\log(V_{seq})$ and M_{main}.

Figure S7b suggests that, for a given mainshock magnitude, MA sequences tend to exhibit smaller V_{seq} values than FMA sequences. The linear fits of the two populations display similar scaling with M_{main}, whereas the MA fit is characterized by a lower intercept. Nevertheless, this apparent difference should be interpreted with caution, as the two populations cannot be considered statistically distinct. Owing to the large variability of V_{seq} within the FMA population, the mean V_{seq} of the MA sequences lies within one standard deviation of the mean V_{seq} of the FMA sequences (Figure S7b).

Relationship between sequence geometry and sequence properties

No clear relationship is observed between sequence type and seismicity geometry (Figure S8a). Among planar sequences, FMA sequences slightly outnumber MA sequences. For sequences with geometrically unconstrained distributions, the proportion of FMA sequences increases to 79%, whereas both linear sequences are classified as MA. The only swarm sequence, which occurred in Stregna (ES) in 2018, exhibits a highly clustered hypocentral distribution and is therefore included in the geometrically unconstrained class, consistent with the occurrence of repeater events in the ES area[33].

A comparison between the logarithm of the number of earthquakes in each sequence and M_{main} shows a clear contrast between planar sequences, which span a broad range of values, and sequences with geometrically unconstrained distributions, the vast majority of which are characterized by fewer than 30 earthquakes and $M_{main} < 3.0$ (Figure S8b).

Comparison between sequence geometry and focal mechanisms

For planar and linear sequences with a mainshock magnitude of $M_L > 2.5$, the orientation of the PCA-derived best-fitting plane was compared with the focal mechanism of the sequence mainshock using the procedure described in the "Methods" section.

Figure S9 shows the distribution of the PCA eigenvectors E_1, E_2, E_3 and the corresponding best-fitting planes obtained from the Monte Carlo simulations together with the nodal planes of the mainshock focal mechanism for each analyzed sequence. This representation illustrates both the uncertainty associated with the PCA-derived orientation and its agreement with the focal mechanism. In particular, the agreement was evaluated through the angle θ_{diff}, defined as the minimum angular difference between the normal to the PCA-derived plane (E3) and the two nodal planes of the focal mechanism.

Overall, 64% of the analyzed sequences exhibit a θ_{diff} smaller than 40° (Figure S10a). The mean θ_{diff} is nearly identical for MA and FMA sequences, with values of 35.3° and 35.4°, respectively. These angular differences are expected because the comparison involves the focal plane of a single earthquake (the mainshock), whose orientation may be affected by uncertainties of several tens of degrees, and the best-fitting plane describing the spatial distribution of the entire seismic sequence, which does not necessarily coincide with the rupture plane of the mainshock. Figure S10b further shows the distribution of θ_{diff} as a function of longitude. Although no clear longitudinal trend is observed, the angular differences appear more scattered in the Western and Central sectors of SEAWD than in the Eastern sector.

Discussion

The detailed relocation and characterization of seismic sequences in the SEAWD area between 2015 and 2024 provide new insights into the spatiotemporal organization of seismicity in one of the most complex tectonic domains of the Eastern Alps–Western Dinarides region. Compared to previous studies based on standard locations and declustering approaches (e.g[42].) the combined application of the rescaled generalized distance and the NLL-SC relocation procedures allows a more robust identification of sequence geometry and depth distribution. A first regional screening of the seismic sequence characteristics suggested predominantly burst-like behavior in the Alpine and pre-Alpine domains and swarm-like activity in the Veneto–Friuli plain (CS area) and along the CS and ES border[42]. High-resolution observations from the temporary Swath-D deployment further identified multiple sequences with both swarm-like and mainshock–aftershock behavior, and revealed short fault structures correlated with zones of high P-wave attenuation[4,43–45].

The spatial distribution of the identified sequences highlights a clear concentration of seismic clustering within the Central SEAWD region, while significantly fewer sequences occur in the western and eastern sectors of SEAWD. The observed spatial variability may reflect not only differences in the regional tectonic setting but also the influence of crustal heterogeneities, attenuation anomalies, fluid circulation, and minor fault structures identified in several sectors of the study area (e.g[46,47]). This pattern likely reflects the structural complexity and heterogeneous stress distribution within the southeastern Alpine–Dinaric transition zone, which was also highlighted by Picozzi et al.[48]. Although not all sequences align exactly with mapped DISS sources, several clusters occur close to the trace of known thrust and strike-slip structures. This suggests that part of the seismicity may illuminate secondary fault segments or portions of larger structures that are not yet fully mapped at or do not reach the surface.

The Central SEAWD corresponds to the region affected by the 1976 Friuli seismic sequence and is characterized by a dense network of south-verging thrust and transpressional structures[49,50] accommodating

the convergence between the Adria microplate and the Eurasian plate. To further investigate the relationship between the relocated seismicity and the active structures, we compared the orientation of the PCA-derived best-fitting plane with the focal mechanisms of the mainshocks, where available. Specifically, we calculated the minimum angular difference (θ_{diff}) between the normal vector to the PCA plane (E_3) and the two nodal planes of the mainshock focal mechanisms for 25 planar and linear sequences with a mainshock magnitude of $M_L > 2.5$. The resulting mean θ_{diff} of 35.5° indicates a first-order consistency between the spatial organization of the seismicity and the deformation style inferred from focal mechanisms, although the relatively large dispersion highlights the complexity of the investigated region. The larger variability observed in the Western and Central sectors of SEAWD compared to the Eastern sector may reflect the more heterogeneous structural framework of these areas, where multiple thrust and transpressional structures are present and the association between individual seismic sequences and mapped fault systems is less straightforward. Overall, these results suggest that the geometry of the relocated sequences is broadly compatible with the regional tectonic framework, while deviations from the focal mechanism orientations likely reflect the effects of fault segmentation, structural complexity, and the limited spatial sampling provided by individual seismic sequences. The concentration of sequences in the Central SEAWD coinciding with the 1976 M_W 6.5 Friuli earthquake area suggests that the present-day microseismicity may still reflect the segmentation and mechanical complexity of the fault system activated during that event. The alignment of many sequences with mapped seismogenic sources from the DISS database suggests that a significant fraction of the observed seismicity occurs along known active fault systems or their associated damage zones. The depth distribution, mostly confined between 5 and 15 km, is consistent with previous estimates of the seismogenic layer thickness in the southeastern Alps[34,48,51] and indicates that these sequences likely activate structures within the upper crustal portion of the Alpine wedge. Previous studies highlighted the mechanical heterogeneity and segmentation that can characterize active fault systems, as revealed by the spatial distribution and clustering of microseismicity[7,8].

In this work, we found a predominance of Foreshock–Mainshock–Aftershock (FMA) and Mainshock–Aftershock (MA) sequences, with a minor contribution of swarm-like activity, which is consistent with the results of Petersen et al.[4], who also reported a limited occurrence of pure swarm sequences in the CS region. The spatial variability between FMA and MA sequences may reflect differences in fault maturity and structural complexity. More mature structures within the Alpine domain may favor the occurrence of dominant mainshocks followed by aftershock sequences, whereas more fragmented fault systems in the pre-Alpine domain may promote preparatory seismic activity preceding the largest event.

This behaviour differs from what has been observed in some sectors of the northwestern Dinarides (Eastern SEAWD), where swarm-like seismicity is relatively common. For example, seismic swarms recorded along the Predjama Fault (Eastern SEAWD) have been interpreted as the result of transient deformation processes, possibly linked to slow slip occurring on the deeper portion of the fault system[33]. On the other hand, in this region we observe highly clustered sequences (included in the not geometrically constrained class) composed of earthquakes with very similar waveforms, which could be interpreted as swarms under classification schemes different from the one adopted in this study. Furthermore, differences in sequence classification in the WS and CS areas compared to previous studies[4,42] may be also related to both the different parameterization of the clustering methods used and the data, which partially coincides or does not coincide with that used in this study. It should also be noted that temporal variations in earthquake detectability may influence the observed number of small events and consequently affect the identification of seismic sequences. However, the study period (2015–2024) postdates the major upgrades of the OGS seismic network and the optimization of the automatic detection procedures completed in 2011[29]. Previous analyses of older versions of the OGS catalogue indicate that the magnitude of completeness remained approximately stable below 1.0 during the last decade[30], suggesting relatively homogeneous earthquake detectability throughout the investigated period. However, we found the magnitude of completeness of the dataset used in this paper to be equal to 0.6 (Figure S1[38,52]). Furthermore, the sequence classification adopted in this study is primarily based on the magnitude difference between the mainshock and the largest preceding event (ΔM) rather than on the total number of detected earthquakes. Therefore, moderate temporal variations in catalogue completeness are not expected to substantially affect the relative proportion of MA, FMA and SW sequences, although the recognition of very small foreshocks may locally be influenced by detectability limits. However, the lower proportion of swarm-like sequences observed in the SEAWD catalogue may indicate that seismic clustering in northeastern Italy is primarily controlled by stress changes associated with moderate mainshocks rather than by aseismic processes. This interpretation is consistent with previous studies showing that the seismicity of the southeastern Alps is influenced by a complex stress field and by the interaction of multiple fault systems (e.g. Bressan et al.[53], Bressan[28]).

In agreement with Petersen et al.[4], we observed a significant percentage of MA sequences in the CS area, where they are more concentrated than in other areas of the SEAWD. However, the higher percentage of FMA sequences identified in this study (65%) suggests that improved relative locations, based on event similarity, enhance the detectability of foreshock activity, which may be partially underestimated by analyzing standard, lower precision catalogues. In particular, the initial regional relocation mitigates uncertainties associated with the velocity model and enables a more reliable selection of candidate sequences. The resulting travel-time residuals indicate that, on average, the observed arrivals are slightly earlier than predicted by the OGS bulletin velocity model, suggesting that the effective propagation velocities sampled by the relocation are somewhat faster, although the same initial velocity model is retained. This behavior is expected when applying SSST corrections, which can compensate for epistemic errors in the velocity model, particularly when a 1D model is used in structurally heterogeneous regions[54].

The predominance of FMA sequences across both Alpine and pre-Alpine domains suggests that earthquake nucleation in the region frequently involves preparatory phases characterized by small precursor activity, which may reflect the progressive loading of complex fault systems. Conversely, MA sequences appear preferentially

concentrated within the Alpine sector of the Central SEAWD, where the fault system is structurally mature and capable of producing more clearly defined mainshock–aftershock patterns. This spatial differentiation may reflect variations in fault maturity, stress regime, and mechanical heterogeneity between the internal Alpine belt and the external thrust-and-fold system toward the foreland.

Some uncertainties remain due to the use of a regional 1D velocity model and to the variable station coverage near the borders of the network. Future analyses based on 3D velocity models and expanded station coverage could further improve the resolution of sequence geometry. Comparing Figs. 1a and 3a, the effect of relocation with NLL-SSST is more evident in depth than in epicentral location. This may be related to the influence of the initial 1D velocity model, which covers an area of approximately 360 × 280 km², on the ability to model lateral heterogeneities in the medium. We expect that relocating the events with a 3D velocity model for SEAWD in the future will result in even more precise epicentral relocation. Subsequent waveform-similarity-based relocation within each sequence further refines their spatial clustering, allowing a more accurate reconstruction of their spatiotemporal evolution. The lack of a clear spatial dominance of a single sequence type, already noted by Petersen et al.[4], is confirmed here. Nevertheless, our results show a tendency for MA sequences to be preferentially located in the Alpine domain of Friuli region (northern part of the CS area), whereas FMA sequences are distributed across both Alpine and pre-Alpine regions in the CS area. This spatial pattern may reflect differences in fault maturity, stress regime, and rheological properties between the internal Alpine belt and the external thrust-and-fold system of Friuli and Veneto (CS area). Interestingly, we found that MA sequences are, on average, characterized by a stronger mainshock than FMA sequences. This suggests that within the SEAWD, foreshock analysis is not significant for forecasting mainshocks with M > 3.5. However, this does not imply that seismic-sequence properties have no predictive value. In the same study area, Brondi et al.[55], showed that the characteristics of the early aftershock activity can successfully forecast the occurrence of subsequent strong aftershocks following an initial strong event. Together, these observations suggest that the predictive information carried by seismic sequences may differ before and after the mainshock. At the same time, geometrically well-constrained FMA sequences systematically exhibit larger characteristic volumes than geometrically well-constrained MA sequences for a given mainshock magnitude, despite the similar scaling between V_{seq} and M_{main}. This systematic offset may indicate that sequences containing foreshock activity undergo a more spatially extended preparatory evolution before the mainshock than sequences initiated directly by the mainshock. Although the underlying physical mechanisms remain to be established, the systematic quantitative characterization of seismic sequences presented in this study opens new opportunities to investigate the physics of rupture preparation and earthquake nucleation across different tectonic settings.

The observed increase in sequence depth toward the Adriatic foreland and eastern Slovenia is consistent with the regional deepening of the seismogenic layer reported in earlier studies and reflects the transition from the Alpine orogenic wedge to the Adriatic indenter[56].

The Principal Component Analysis performed on the spatial distribution of events within each sequence reveals that most clusters exhibit a planar geometry, while a smaller fraction appears geometrically not constrained and only a few sequences display a linear structure. Planar distributions of hypocentres are commonly interpreted as reflecting the activation of fault planes or damage zones surrounding them. The predominance of planar geometries in our dataset therefore suggests that most sequences likely occur along well-defined structural planes within the seismogenic crust. In contrast, highly clustered sequences likely reflect small asperities or limited rupture patches within the fault network. The few linear sequences identified in our analysis show near-vertical trends. Bressan et al.[28], using PCA and fractal dimension analyses, also found vertical distributions of seismicity in the CS area; however, these appear to have a much higher incidence than observed in our work.

The relationship observed between the logarithm of the estimated sequence volume V_{seq} and the magnitude of the mainshock suggests a first-order scaling between the spatial extent of clustered seismicity and the size of the largest event. Although the volume derived from the PCA analysis represents only a first-order measurement for the true rupture sequence volume, the observed trend is consistent with empirical scaling relationships between rupture dimensions and earthquake magnitude documented in many tectonic environments. In this context, larger mainshocks are expected to activate wider portions of the surrounding fault network, generating broader aftershock clouds and larger seismic clusters. The variability observed within this relationship may reflect differences in fault-zone structure, mechanical heterogeneity, or stress conditions across the SEAWD region. Furthermore, this scaling could be partly explained by the diffusion of fluids observed in the SEAWD area, related to the occurrence of a moderate-intensity mainshock that creates transient deformation and modulates background seismicity[27]. Fluid diffusion processes may, in fact, contribute to the observed clustering behaviour. Transient increases in pore pressure can locally reduce effective normal stress on faults, promoting the activation of small clusters of earthquakes even in the absence of large stress perturbations.

The absence of a clear relationship between sequence type and the spatial geometry of seismicity suggests that the temporal evolution of earthquake clusters may be largely independent from the structural geometry of the activated fault zone. Numerical and statistical models of earthquake triggering have shown that foreshock, aftershock, and swarm sequences can emerge from the same cascading stress-transfer processes within complex fault networks (e.g[57–59]).

Overall, this study confirms and refines previous findings while demonstrating that high-precision relocation and geometrical analysis significantly improve our understanding of seismic sequence behavior. Even though most sequences involve small-to-moderate earthquakes, their spatial organization provides valuable constraints on the geometry of active fault structures that may host larger future earthquakes. High-precision sequence locations provide indirect constraints on the geometry of active structures that may not be fully resolved at the surface. Such information can contribute to improving the characterization of seismogenic sources and therefore to refining regional seismic hazard models. The ability to rapidly identify and characterize seismic sequences

using clustering and relocation techniques may provide valuable information for operational seismic monitoring, particularly in regions such as northeastern Italy where moderate earthquakes can generate damaging ground shaking.

Data

This study analyzes approximately 17,000 seismic events recorded between 2015 and 2024 and included in the seismic bulletins published by the National Institute of Oceanography and Experimental Geophysics – OGS (Fig. 1a). The progressive evolution of the OGS seismic network, particularly in terms of station density and operational performance, has significantly influenced the magnitude of completeness (Mc) of the catalogue over time[60]. Over the last 15 years, the coverage provided by the Struttura di Monitoraggio dell'Italia Nord Orientale (SMINO) network[29] has allowed the achievement of a Mc below 1 in the Friuli Venezia Giulia region[55]. The dataset used in the paper presents Mc equal to 0.6 (Figure S1).

Since its establishment in 1977, the SMINO network has supported the compilation of annual seismic bulletins by OGS, which are publicly available online. The dataset used in this study includes events published in the bulletins from 2015 to 2023[61–69]; https://www.crs.ogs.it/bollettino_new/), as well as events recorded in 2024 and reviewed by the Review Group of the Seismological Research Center (CRS, https://terremoti.ogs.it/) of the National Institute of Oceanography and Experimental Geophysics – OGS. These bulletins include manually reviewed phase picks from stations operated by OGS and collaborating institutions in Italy and Europe.

In this study, we used data from approximately 150 seismic stations (Fig. 1a). For Italy, the dataset includes stations belonging to networks managed by the CRS [international code OX[70]]; the North-East Italy Broadband Network [international code NI[71]]; the Italian National Seismic Network [international code IV[72]]; the Collalto Seismic Network [international code EV[73]]; the Friuli Venezia Giulia Accelerometric Network [international code RF[74]]; the Trentino Seismic Network [international code ST[75]]; the Province Südtirol Seismic Network [international code SI]; the Mediterranean Very Broadband Seismographic Network [international code MN[76]]; and the Interreg IV HAREIA project [hereinafter HA[74]] (Fig. 1b). Additional data were obtained from the Austrian Seismic Network [international code OE, GeoSphere, ZAMG – Central Institute for Meteorology and Geodynamics[77]], the Seismic Network of the Republic of Slovenia [international code SL, Agency of the Republic of Slovenia for the Environment (ARSO)[78]], the Croatian Seismograph Network [international code CR, University of Zagreb[79]], and the Swiss National Seismic Network [Swiss Seismological Service (SED) at ETH Zurich[80]] (Fig. 1b).

These collaborations are essential for obtaining accurate earthquake locations, particularly near the edges of the network, where the availability of additional stations helps reduce azimuthal gaps to values below 180° and ensures a typical depth uncertainty of about 2 km[29]. Hypocentral locations are computed using the HYPO71 algorithm[81], adopting a regional velocity model and parameterization specifically developed for the study area[34]. For each seismic event, the bulletin reports the duration magnitude (M_D), calculated using the empirical relationships proposed by Rebez and Renner[82] and calibrated to be consistent with the local magnitude (M_L) derived from the Wood–Anderson seismograph installed in Trieste[83].

Methods

Methodological workflow

We followed a multi-step procedure to identify seismic sequences and accurately relocate them using the NLL-SC technique[35,84](Fig. 2). This algorithm has been adapted to enhance relative location precision by incorporating spatially variable, source-specific station travel-time corrections (SSST) and a multi-event relocation strategy based on waveform coherence (NLL-SC[35]). This method builds upon the NonLinLoc (NLL) probabilistic global-search algorithm[85,86], which estimates hypocenter locations by constructing a three-dimensional probability density function (PDF). This approach is particularly robust to the presence of outliers in the input data[35] and was used to obtain high-resolution location data for volcanic[87] and tectonic[10] structures.

In our procedure, using data from the OGS bulletin and monitoring group catalogue, we relocated the entire catalogue with the initial NLL-SSST procedure. Then, the relocated catalogue has been used to identify seismic sequences by applying the nearest-neighbour method[37,39]. After identifying the sequences, we applied a second relocation analysis to each of them based on waveform coherence with NLL-coherence (Fig. 2). The relocated sequences were then classified according to their temporal evolution (FMA, MA or SW) and characterized in terms of their spatial geometry and sequence volume using Principal Component Analysis (PCA), with uncertainties quantified through Monte Carlo uncertainty propagation. Since HYPO71 and NLL use a perturbative and probabilistic approach for location, respectively, we verified with a preliminary test that, to a first approximation, the two methods reproduce the same results using the 1D velocity model with V_P/V_S=1.78 used for the OGS bulletin[34]. In addition, we conducted a localization test with NLL, comparing the previous velocity model with two more complex 1D models for SEAWD: the 1D velocity model by Gentile et al.[88], and a 1D velocity profile derived from the 3D model by Magrin and Rossi[89]. Comparing the residual distributions of P- and S-wave arrivals at stations, the model by Slejko et al.[34], showed the best performance. The detailed comparison of the P- and S-wave travel-time residual distributions obtained with the three velocity models for four representative OX network stations is provided in Figures S11 and S12, respectively.

SSST analysis

We initially relocated the 2015–2024 OGS seismic catalogue iteratively while generating smoothly varying SSST corrections throughout a three-dimensional volume with dimensions of 360 km in longitude, 280 km in latitude, 45 km in depth, and using a constant spatial step of 0.5 km. These corrections, dependent on the position of the events relocated in the previous iteration, are computed for P- and S-wave seismic phases of 83 seismic stations. Considering that the study area extends over approximately 360 km x 280 km, six iterations

were required to progressively reduce the SSST correlation length from regional to cluster-scale dimensions. In this NLL-SSST analysis, at each iteration, only residuals from P- and S-phase picks and events that meet a fixed quality threshold are utilized for the updates[35]. The final refined NLL-SSST locations have been obtained by the application of the Gaussian SSST smoothing kernels with progressively smaller widths which correspond to the smoothing distances of 32, 16, 8, 4, and 2 km. The quality criteria for location and station-phase to be used for calculating are: 68% error-ellipsoid principle-axis half-width ≤ 5.0 km, root mean square of residuals (RMS) ≤ 0.15 s, number of readings ≥ 10, azimuth gap ≤ 120°, P-phase residual ≤ 0.5 s, S-phase residual ≤ 1.0 s.

Clustering by nearest-neighbour distance, η

The catalogue obtained from the SSST analysis is used to identify the main sequences that occurred between 2015 and 2024 in our study area using the clustering method of Zaliapin et al.[36]. This approach computes the generalized distance between pairs of earthquakes, η, by an analysis of the time-space distances between pairs of earthquakes, which consists in estimating the distances in time (i.e., rescaled time, T_η) and space (i.e., rescaled distance, R_η) between an event i and its parent j, where both distances are normalized by the magnitude of the parent event.

Rescaled time and distance are computed as follows:

$$T_{ij} = t_{ij} 10^{-b\frac{m_i}{2}} \tag{1}$$

$$R_{ij} = (r_{ij})^{D_c} 10^{-b\frac{m_i}{2}} \tag{2}$$

where, m is the magnitude, b is the parameter of the Gutenberg–Richter law, which plays the role of exponential weight of the earlier event i by its magnitude, and D_c is the fractal dimension. Finally, η is defined as:

$$log\,(\eta_{ij}) = log(R_{ij}) + log(T_{ij}) \tag{3}$$

Following Zaliapin and Ben-Zion[37], we set the b equal to 0 to mitigate the presence of artifacts due to the overlap of earthquakes' domain of attraction with background seismicity, and we use D_c equal to 1.5. To create a family of events (i.e., a cluster) we required a minimum number of events equal to 10.

Waveform based analysis

In this stage, the relative precision of the NLL-SSST event locations is further refined by integrating waveform similarity across events for each sequence. This second relocation step, NLL-coherence, relies on the principle that, when seismograms from different events show strong similarity at a given station—i.e., high coherence across a broad frequency band—the spatial separation between such "multiplet" events must be small compared to the seismic wavelength at the highest coherent frequency[35]. These events are likely to represent slip on the same, localized fault patch[90–93].

For our NLL-coherence relocations, we calculated the coherence using channel data from the horizontal and vertical components of velocimeter sensors located around the immediate vicinity of the sequence. In particular, in order to ensure a good azimuthal coverage of the stations around the seismicity cluster of each sequence, we decided to use a minimum of 4 stations up to a maximum of 8 stations located around the midpoint of the epicentral distribution of the sequence. In calculating coherence, according to Lomax and Savvaidis[35] we applied a 2–10 Hz bandpass filter in a signal window starting 4 s before the arrival of the predicted P-wave and ending 4 s after the theoretical arrival of the S-wave. We perform cross-correlation on waveform windows that slide within the range from − 4.0 to 4.0 s. Stacking weights, ranging from 0 to 1, are assigned based on the NLL-SC procedure of Lomax and Savvaidis[35] and applied to coherency values between Cmin = 0.5 and 1.0. This method is implemented for the D = 2 km NLL-SSST relocations of the 71 sequences of SEAWD, considering all event pairs whose hypocentral distance does not exceed 5.0 km.

Principal component analysis, sequence volume estimation and uncertainty propagation

To characterize the spatial geometry of the seismic sequences and quantify the uncertainty associated with the estimated sequence volume and geometry, we combined Principal Component Analysis (PCA) with a Monte Carlo uncertainty propagation approach.

To reduce the influence of poorly constrained hypocentres and isolated outliers, a two-step event selection procedure was first applied. Earthquakes characterized by horizontal or vertical location uncertainties larger than 2 km were discarded. Subsequently, for each sequence, we identified the smallest cylinder centred on the median hypocentre, with radius r_{perc} and height $2r_{perc}$, enclosing at least 90% of the earthquakes. Only the selected events were retained for the subsequent analyses.

An initial estimate of the reference sequence volume ($V_{seq}{}^0$) was computed as the three-dimensional Delaunay convex hull of the relocated NLL-SC maximum probability hypocentres using the PyCEFeaX package[38,94]. Sequences characterized by null or negligible $V_{seq}{}^0$ values were not considered in the uncertainty propagation analysis and were classified as geometrically unconstrained.

To quantify the effect of location uncertainties on both the estimated sequence volume and the PCA geometry, we generated 100 Monte Carlo realizations for each earthquake by sampling from the multivariate normal distribution defined by the preferred NLLoc hypocentre and its associated covariance matrix. However, because the waveform-coherence relocation constrains the final hypocentral configuration through coherence-weighted stacking of the event-specific probability density functions, the covariance matrix associated with each earthquake represents only its marginal absolute-location uncertainty and does not retain the pseudo-relative

dependence among neighbouring events. Consequently, independent sampling would artificially broaden the synthetic catalogues and systematically overestimate the sequence volume. To preserve the pseudo-relative clustering resolved by the waveform-coherence relocation, each Monte Carlo realization was therefore adjusted using a coherence-weighted correction that mimicked the PDF-stacking principle adopted by the NLL-SC relocation procedure. The correction combines the independently sampled hypocentral position with the coherence-weighted contribution of the neighbouring earthquakes, while a sequence-specific parameter, β, controls the relative weight assigned to the two contributions:

$$x_i^{(1)} = (1 - \beta) * x_i^{(0)} + \beta \sum_j (\omega_{ij} x_j^{(0)}) \quad (4)$$

where **i** and **j** denote earthquakes belonging to the same sequence, $\boldsymbol{\omega_{ij}}$ represents the normalized waveform-coherence weight between earthquakes *i* and *j*, and β controls the strength of the coherence correction.

The parameter β was optimized independently for each sequence by requiring that the median sequence volume (V_{seq}) obtained from the Monte Carlo realizations matched the reference volume (V_{seq}^{0}) computed from the preferred NLL-SC hypocentral configuration. This optimization accounts for the fact that the effectiveness of the coherence-weighted correction depends on the characteristics of the individual sequence, including its spatial extent, geometry, event density, location uncertainties, and the distribution of waveform-coherence weights. Under this assumption, the preferred NLL-SC hypocentral configuration is regarded as the reference pseudo-relative solution, whereas the Monte Carlo ensemble quantifies the uncertainty associated with this configuration by propagating the event-specific location uncertainties while preserving, on average, the pseudo-relative clustering resolved by the waveform-coherence relocation.

Sequence volume and PCA were recomputed for every Monte Carlo realization. Since the resulting V_{seq} distributions were found to be approximately log-normal, sequence volumes and their associated uncertainties were estimated using log-normal statistics.

PCA was performed on the hypocentral coordinates expressed in a local Cartesian reference system using the PyCEFeaX package, which implements a singular value decomposition based on the LAPACK library[95]. Each realization yielded three orthogonal eigenvectors (E_1, E_2 and E_3) with their corresponding eigenvalues (λ_1, λ_2 and λ_3).

To derive a representative PCA solution for each sequence, every Monte Carlo realization was first converted into its covariance operator. The covariance operators were then averaged over all realizations and eigendecomposed, yielding representative principal components and associated variances for the Monte Carlo ensemble.

Sequences were classified according to the ratios between the PCA eigenvalues λ_1, λ_2 and λ_3[98,99] together with the estimated sequence volume:

$$PCA\ classification \begin{cases} planar & : \frac{\lambda_1}{\lambda_3} > 2.5,\ \frac{\lambda_2}{\lambda_3} > 1.75,\ V_{seq} \gg 0 \\ linear & : \frac{\lambda_1}{\lambda_3} > 2.5,\ \frac{\lambda_2}{\lambda_3} \leq 1.75,\ V_{seq} \gg 0 \\ not\ constrained & : \frac{\lambda_1}{\lambda_3} \leq 2.5,\ \frac{\lambda_2}{\lambda_3} \leq 1.75 \end{cases} \quad (5)$$

For each Monte Carlo realization, the PCA eigenvalue ratios (λ_1/λ_3 and λ_2/λ_3) were recomputed, yielding empirical uncertainty distributions. For sequences with non-zero V_{seq}, the probabilities of belonging to the planar, linear, and geometrically unconstrained classes (P(PL), P(LI), and P(NC), respectively; see Supplementary Table 2) were estimated as the fraction of Monte Carlo realizations satisfying the corresponding classification criteria defined by Eq. (5). Conversely, for sequences with negligible V_{seq}, no meaningful PCA classification probabilities can be defined because the sequence geometry is insufficiently resolved. These sequences were therefore directly assigned to the geometrically unconstrained class.

Finally, for planar and linear sequences with a mainshock magnitude of $M_L > 2.5$, the orientation of the best-fitting PCA plane was compared with the focal mechanism of the sequence mainshock reported in the regional focal-mechanism catalogues[31,96,97]. The comparison was performed through the angle θ_{diff}, defined as the minimum angular difference between the normal to the PCA-derived plane (E_3) and the two nodal planes of the focal mechanism.

Data availability

The seismic catalogue analyzed in this study is derived from the seismic bulletins of the National Institute of Oceanography and Experimental Geophysics – OGS, produced by the Seismological Research Center (CRS) within the Struttura di Monitoraggio dell'Italia Nord Orientale (SMINO). The bulletins for the period 2015–2023 are publicly available at https://www.crs.inogs.it/bollettino_new/. The dataset for 2024, reviewed by the CRS, is publicly available at https://terremoti.ogs.it/.

Received: 19 March 2026; Accepted: 24 August 2026

References

1. Adinolfi, G. M. et al. Comprehensive study of micro-seismicity by using an automatic monitoring platform. *Front. Earth Sci.* **11**, 1073684. https://doi.org/10.3389/feart.2023.1073684 (2023).

2. Mousavi, S. M., Ellsworth, W. L., Zhu, W., Chuang, L. Y. & Beroza, G. C. Earthquake transformer—an attentive deep-learning model for simultaneous earthquake detection and phase picking. *Nat. Commun.* **11**(1), 3952. (2020).
3. Tan, Y. J. et al. Machine-learning-based high-resolution earthquake catalog reveals how complex fault structures were activated during the 2016–2017 central Italy sequence. *Seism. Rec.* https://doi.org/10.1785/0320210001 (2021).
4. Petersen, G. M., Hofman, L. J., Kummerow, J. & Cesca, S. Microseismicity in the large-N Swath-D network: Revealing seismic sequences and active faults in the eastern Alps. *J. Geoph Res. : Solid Earth*. **130**, e2024JB030516. https://doi.org/10.1029/2024JB030516 (2025).
5. Liu, Y.-K., Ross, Z. E., Cochran, E. S. & Lapusta, N. A unified perspective of seismicity and fault coupling along the San Andreas fault. *Sci. Adv.* **8**, eabk1167 (2022).
6. Muzellec, T., De Landro, G., Camanni, G., Adinolfi, G. M. & Zollo, A. The complex 4D multi-segmented rupture of the 2014 Mw 6.2 Northern Nagano Earthquake revealed by high-precision aftershock locations. *Tecto* **898**, 230641 (2025).
7. Picozzi, M., Bindi, D., Zollo, A., Festa, G. & Spallarossa, D. Detecting long-lasting transients of earthquake activity on a fault system by monitoring apparent stress, ground motion and clustering. *Sci. Rep.* **9**, 16268. https://doi.org/10.1038/s41598-019-52756-8 (2019).
8. Picozzi, M., Spallarossa, D., Bindi, D., Iaccarino, A. G. & Rivalta, E. Detection of spatial and temporal stress changes during the 2016 central Italy seismic sequence by monitoring the evolution of the energy index. *J. Geoph Res. : Solid Earth*. **127**, e2022JB025100. https://doi.org/10.1029/2022JB025100 (2022).
9. Poggiali, G., Chiaraluce, L., Ross, Z. E., Zhu, W. & Marone, C. Fault Geometry and Source Mechanics of the Altotiberina Fault System from a High-Resolution Machine-Learning Earthquake Catalog. *Bull. Seismol. Soc. Am.* **115**, 2181–2201. https://doi.org/10.1785/0120250072 (2025).
10. Sollai, A. et al. High-precision earthquake locations reveal detailed fault geometries in the western Corinth Rift. In *EGU General Assembly Conference Abstracts*, EGU25-21500 (2025).
11. Riga, G. & Balocchi, P. Seismic sequence structure and earthquakes triggering patterns. *Open. J. Earthq. Res.* **5**, 20–34 (2015).
12. King, G. C. P., Stein, R. S. & Lin, J. Static stress changes and the triggering of earthquakes. *Bull. Seism Soc. Am.* **84**, 935–953. https://doi.org/10.1785/BSSA0840030935 (1994).
13. Nandan, S., Ouillon, G., Woessner, J., Sornette, D. & Wiemer, S. Systematic assessment of the static stress-triggering hypothesis using inter-earthquake time statistics. *J. Geophys. Res. Solid Earth* **122**, 6271–6291 (2017).
14. Stein, R. S. The role of stress transfer in earthquake occurrence. *Nature* https://doi.org/10.1038/45144 (1999).
15. Jia, Z. et al. The complex dynamics of the 2023 Kahramanmaraş, Turkey, Mw 7.8–7.7 earthquake doublet. *Science* **381**, 985–990. https://doi.org/10.1126/science.adi0685 (2023).
16. Shelly, D. R., Skoumal, R. J. & Hardebeck, J. L. Fracture-mesh faulting in the swarm-like 2020 Maacama sequence revealed by high-precision earthquake detection, location, and focal mechanisms. *Geophys. Res. Lett.* https://doi.org/10.1029/2022GL101233 (2023).
17. Michele, M., Chiaraluce, L., Di Stefano, R. & Waldhauser, F. Fine-scale structure of the 2016–2017 Central Italy seismic sequence from data recorded at the Italian National Network. *J. Geophys. Res. Solid Earth* **125**, e2019JB018440 (2020).
18. Picozzi, M. et al. A rapid response magnitude scale for timely assessment of the high frequency seismic radiation. *Sci. Rep.* **8**, 8562. https://doi.org/10.1038/s41598-018-26938-9 (2018).
19. Picozzi, M. et al. Event-specific ground motion anomalies highlight the preparatory phase of earthquakes during the 2016–2017 Italian seismicity. *Commun. Earth Environ.* **5**, 289. https://doi.org/10.1038/s43247-024-01455-y (2024).
20. Camanni, G. et al. Remobilization of inverted normal faults drives active extension in the axial zone of the southern Apennine mountain belt (Italy). *J. Geol. Soc.* **182**(2), jgs2024-184 (2025).
21. Gentili, S. et al. Seismic clusters and fluids diffusion: a lesson from the 2018 Molise (Southern Italy) earthquake sequence. *Earth Plan. Spa*. **76**, 157. https://doi.org/10.1186/s40623-024-02096-3 (2024).
22. Palo, M., Picozzi, M., De Landro, G. & Zollo, A. Microseismicity clustering and mechanic properties reveal fault segmentation in southern Italy. *Tectons* **856**, 229849 (2023).
23. di Scotto, F. et al. Delineation and fine-scale structure of fault zones activated during the 2014–2024 unrest at the Campi Flegrei caldera (Southern Italy) from high- precision earthquake locations. *Geophys. Res. Lett.* https://doi.org/10.1029/2023GL107680 (2024).
24. Vuan, A. et al. Intermittent slip along the Alto Tiberina low-angle normal fault in central Italy. *Geophys. Res. Lett.* https://doi.org/10.1029/2020GL089039 (2020).
25. Bressan, G., Gentile, G. F., Perniola, B. & Urban, S. The 1998 and 2004 Bovec-Krn (Slovenia) seismic sequences:Aftershock pattern, focal mechanisms and static stress changes. *Geophys. J. Int.* **179**, 231–253 (2009).
26. Bressan, G., Barnaba, C., Magrin, A. & Rossi, G. A study on off-fault aftershock pattern N-Adria microplate. *J. Seism*. **22**, 863–888. https://doi.org/10.1007/s10950-018-9737-x (2018).
27. Rossi, G., Pastorutti, A., Nagy, I., Braitenberg, C. & Parolai, S. Recurrence of fault valve behavior in a continental collision area: Evidence from tilt/strain measurements in Northern Adria. *Front. Earth Sci.* **9**, 641416. https://doi.org/10.3389/feart.2021.641416 (2021).
28. Bressan, G., Barnaba, C., Peresan, A. & Rossi, G. Anatomy of seismicity clustering from parametric space-time analysis. *Phys. Earth Plan. Int.* **320**, 106787 (2021).
29. Bragato, P. L. et al. The OGS–northeastern Italy seismic and deformation network: Current status and outlook. *Seism Res. Lett.* **92**, 1704–1716. https://doi.org/10.1785/0220200372 (2021).
30. Sandron, D., Rebez, A., Tamaro, A., Slejko, D. Recent earthquakes (2000–2021) in and around the Friuli Venezia Giulia region (NE Italy) and quality improvements of the OGS network monitoring capabilities. *Bull. Geoph. Ocean*. https://doi.org/10.4430/bgo00421 (2023).
31. Saraò, A., Sugan, M., Bressan, G., Renner, G. & Restivo, A. A focal mechanism catalogue of earthquakes that occurred in the southeastern Alps and surrounding areas from 1928–2019. *Earth Syst. Sci. Data*. **13**, 2245–2258 (2021).
32. Atanackov, J. et al. Database of active faults in Slovenia: Compiling a new active fault database at the junction between the Alps, the Dinarides and the Pannonian Basin tectonic domains. *Front. Earth Sci.* **9**, 604388 (2021).
33. Vičič, B., Aoudia, A., Javed, F., Foroutan, M. & Costa, G. Geometry and mechanics of the active fault system in western Slovenia. *Geophys. J. Int.* https://doi.org/10.1093/gji/ggz118 (2019).
34. Slejko, D. et al. Seismotectonics of the Eastern Southern Alps: a review. *Boll Geofis. Teor Appl*, **31**(122) (1989).
35. Lomax, A. & Savvaidis, A. High-precision earthquake location using source-specific station terms and inter-event waveform similarity. *J. Geophys. Res. Solid Earth* **127**, e2021JB023190 (2022).
36. Zaliapin, I., Gabrielov, A., Keilis-Borok, V. & Wong, H. Clustering analysis of seismicity and aftershock identification. *Phys. Rev. Lett*. **101**, 018501 (2008).
37. Zaliapin, I. & Ben-Zion, Y. Earthquake declustering using the nearest-neighbor approach in space-time-magnitude domain. *Journal of Geophysical Research: Solid Earth* https://doi.org/10.1029/2018JB017120 (2020).
38. Iaccarino, A. G. & Picozzi, M. PyCEFeaX. *Zenodo* https://doi.org/10.5281/zenodo.18548970 (2026).
39. Zaliapin, I. & Ben-Zion, Y. Earthquake clusters in southern California I: identification and stability. *J. Geophys. Res. Solid Earth*. https://doi.org/10.1002/jgrb.50179 (2013).

40. DISS Working Group. Database of Individual Seismogenic Sources (DISS), version 3.3.1: A compilation of potential sources for earthquakes larger than M 5.5 in Italy and surrounding areas. Istituto Nazionale di Geofisica e Vulcanologia (INGV). https://doi.org/10.13127/diss3.3.1 (2025).
41. Ogata, Y. & Katsura, K. Prospective foreshock forecast experiment during the last 17 years. *Geoph Jour Inte*. https://doi.org/10.1111/j.1365-246X.2012.05645.x (2012).
42. Peresan, A. & Gentili, S. Seismic clusters analysis in Northeastern Italy by the nearest-neighbor approach. *Phys. Earth Plan. Int.* **274**, 87–104 (2018).
43. Heit, B. et al. The Swath-D seismic network in Italy and Austria. *GFZ Data Serv.* https://doi.org/10.14470/mf7562601148 (2017).
44. Heit, B. et al. The SWATH-D seismological network in the eastern Alps. *Seism Res. Lett.* **92**, 1592–1609. https://doi.org/10.1785/0220200377 (2021).
45. Hofman, L. J., Kummerow, J. & Cesca, S. the AlpArray-Swath-D Working Group. A new seismicity catalogue of the eastern Alps using the temporary Swath-D network. *Solid Earth*. **14**, 1053–1066. https://doi.org/10.5194/se-14-1053-2023 (2023).
46. Jozi et al. Seismic wave attenuation (1/*Qp*) in the crust underneath the Eastern and eastern Southern Alps (Europe): imaging effects of faults, fractures, and fluids. *Earth Planet Space*. **75**, 187. https://doi.org/10.1186/s40623-023-01942-0 (2023).
47. Talone, D. et al. Underground Gas Storage as benchmark for seismic attenuation tomography in a tectonically complex region (north-eastern Italy). *Geophys. Res. Lett.* https://doi.org/10.1029/2025GL117956 (2025).
48. Picozzi, M. et al. Seismic energy from small earthquakes maps fault segmentation in the Southeastern Alps. *Sci. Rep.* **16**, 5731. https://doi.org/10.1038/s41598-026-35618-y (2026).
49. Marchesini, A. et al. *Linee guida per l'utilizzo della banca dati georiferita delle faglie attive della Regione Friuli Venezia Giulia* 64 (Servizio Geologico - Regione Autonoma Friuli Venezia Giulia, 2023).
50. Poli, M. E., Patricelli, G., Monegato, G. & Zanferrari, A. Structural inheritances, fault segmentation and seismogenic potential at the front of the eastern Southern Alps (central Carnic Prealps, NE Italy). *Tecton* **883**, 230390 (2024).
51. Viganò, A. et al. Earthquake relocations, crustal rheology, and active deformation in the central–eastern Alps (N Italy). *Tecton* https://doi.org/10.1016/j.tecto.2015.08.017 (2015).
52. Wiemer, S. A software package to analyze seismicity: ZMAP. *Seismol. Res. Lett.* https://doi.org/10.1785/gssrl.72.3.373 (2001).
53. Bressan, G., Barnaba, C., Bragato, P., Ponton, M. & Restivo, A. Revised seismotectonic model of NE Italy and W Slovenia based on focal mechanism inversion. *J. Seism.* **22**, 1563–1578 (2018).
54. Lomax, A., Tuvè, T., Giampiccolo, E. & Cocina, O. A new view of seismicity under Mt. Etna volcano, Italy, 2014–2023 from multi-scale high-precision earthquake relocations. *Annals Geoph*. **67**, S437–S437 (2024).
55. Brondi, P., Gentili, S. & Di Giovambattista, R. Forecasting strong subsequent events in the Italian territory: a national and regional application for NESTOREv1.0. *Nat. Hazards*. **121**, 3499–3531. https://doi.org/10.1007/s11069-024-06913-6 (2025).
56. Zupančič, P. et al. Seismogenic depth and seismic coupling estimation in the transition zone between Alps, Dinarides and Pannonian Basin for the new Slovenian seismic hazard model. *Nat. Hazards Earth Syst. Sci.* **24**, 651–672. https://doi.org/10.5194/nhess-24-651-2024 (2024).
57. Helmstetter, A. & Sornette, D. Subcritical and supercritical regimes in epidemic models of earthquake aftershocks. *J. Geophys. Res. Solid Earth*. **107**, ESE–10 (2002).
58. Im, K. & Avouac, J. P. Cascading foreshocks, aftershocks and earthquake swarms in a discrete fault network. *Geophys. J. Int.* **235**, 831–852 (2023).
59. Saichev, A. & Sornette, D. Anomalous power law distribution of total lifetimes of branching processes: Application to earthquake aftershock sequences. *Phys. Rev. E* **70**, 046123 (2004).
60. Gentili, S., Sugan, M., Peruzza, L. & Schorlemmer, D. Probabilistic completeness assessment of the past 30 years of seismic monitoring in northeastern Italy. *Phys. Earth Plan. Int.* **186**, 81–96 (2011).
61. Brondi, P., Snidarcig, A., Bernardi, P., Bragato, P. L. & Di Bartolomeo, P. Bollettino della Rete Sismometrica dell'Italia Nord Orientale (RSINO), Anno 2022 [Data set]. Istituto Nazionale di Oceanografia e di Geofisica Sperimentale - OGS. https://doi.org/10.13120/w1vp-b578 (2024).
62. Brondi, P. et al. Bollettino della Rete Sismometrica dell'Italia Nord Orientale (RSINO), Anno 2023 [Data set]. Istituto Nazionale di Oceanografia e di Geofisica Sperimentale - OGS. DOI: https://doi.org/10.13120/m4pk-nd81 (2025).
63. Snidarcig, A. et al. Bollettino della Rete Sismometrica dell'Italia Nord Orientale (RSINO), Anno 2015 [Data set]. Istituto Nazionale di Oceanografia e di Geofisica Sperimentale - OGS. https://doi.org/10.6092/d07746ca-463e-408c-9b98-1063baf66a73 (2016).
64. Snidarcig, A. et al. Bollettino della Rete Sismometrica dell'Italia Nord Orientale (RSINO), Anno 2016 [Data set]. Istituto Nazionale di Oceanografia e di Geofisica Sperimentale - OGS. https://doi.org/10.6092/a608d853-755e-4177-aada-992857ccb44e (2017).
65. Snidarcig, A. et al. Bollettino della Rete Sismometrica dell'Italia Nord Orientale (RSINO), Anno 2017 [Data set]. Istituto Nazionale di Oceanografia e di Geofisica Sperimentale - OGS. (2018). https://doi.org/10.6092/3ff3c323-d7a4-4183-bea0-1a53814ac8b9
66. Snidarcig, A. et al. Bollettino della Rete Sismometrica dell'Italia Nord Orientale (RSINO), Anno 2018 [Data set]. Istituto Nazionale di Oceanografia e di Geofisica Sperimentale - OGS. https://doi.org/10.6092/c53f37ce-bcf3-453c-a2cf-1894d48cfbbb (2019).
67. Snidarcig, A. et al. Bollettino della Rete Sismometrica dell'Italia Nord Orientale (RSINO), Anno 2019 [Data set]. Istituto Nazionale di Oceanografia e di Geofisica Sperimentale - OGS. https://doi.org/10.6092/58ff169a-2f02-46ae-908a-bdfcacea069c (2020).
68. Snidarcig, A. et al. Bollettino della Rete Sismometrica dell'Italia Nord Orientale (RSINO), Anno 2020 [Data set]. Istituto Nazionale di Oceanografia e di Geofisica Sperimentale - OGS. https://doi.org/10.13120/108b8d94-361a-45f3-8195-fc4e8f73d264 (2021).
69. Snidarcig, A. et al. Bollettino della Rete Sismometrica dell'Italia Nord Orientale (RSINO), Anno 2021 [Data set]. Istituto Nazionale di Oceanografia e di Geofisica Sperimentale - OGS. https://doi.org/10.13120/8b252b09-314f-456f-812a-b05268ecd001 (2022).
70. Istituto Nazionale di Oceanografia e di Geofisica Sperimentale – OGS North-East Italy Seismic Network. Data set. International Federation of Digital Seismograph Networks. https://doi.org/10.7914/SN/OX (2016).
71. Istituto Nazionale di Oceanografia e di Geofisica Sperimentale, University of Trieste. North-East Italy Broadband Network [Data set]. *Int. Federation Digit. Seismogr. Networks*. https://doi.org/10.7914/SN/NI (2002).
72. Istituto Nazionale di Geofisica e Vulcanologia (INGV). Rete Sismica Nazionale (RSN) [Data set]. *Istituto Naz. di Geofis. e Vulcanologia (INGV)*. https://doi.org/10.13127/sd/x0fxnh7qfy (2005).
73. Priolo, E. et al. Seismic monitoring of an underground natural gas storage facility: The Collalto seismic network. *Seism Res. Lett.* **86**, 109–123. https://doi.org/10.1785/0220140087 (2015).
74. University of Trieste. Friuli Venezia Giulia Accelerometric Network [Data set]. International Federation of Digital Seismograph Networks. https://doi.org/10.7914/SN/RF (1993).
75. Geological Survey-Provincia Autonoma di Trento. Trentino Seismic Network [Data set]. International Federation of Digital Seismograph Networks. https://doi.org/10.7914/SN/ST (1981).
76. MedNet Project Partner Institutions. Mediterranean Very Broadband Seismographic Network (MedNet) [Data set]. Istituto Nazionale di Geofisica e Vulcanologia (INGV). https://doi.org/10.13127/SD/FBBBTDTD6Q (1990).
77. ZAMG - Zentralanstalt für Meterologie und Geodynamik. Austrian Seismic Network [Data set]. International Federation of Digital Seismograph Network. https://doi.org/10.7914/SN/OE (1987).
78. Slovenian Environment Agency. Seismic Network of the Republic of Slovenia [Data set]. *I*International Federation of Digital Seismograph Networks. https://doi.org/10.7914/SN/SL (1990).
79. University of Zagreb. Croatian Seismograph Network. [Data set]. *Int. Federation Digit. Seismogr. Networks*. https://doi.org/10.7914/SN/CR (2001).

80. Swiss Seismological Service (SED). At ETH Zurich. National Seismic Networks of Switzerland. *ETH Zürich*. https://doi.org/10.12686/sed/networks/ch (1983).
81. Lee, W. H. & Lahr, J. C. *HYPO71 (revised; a computer program for determining hypocenter, magnitude, and first motion pattern of local earthquakes* (No. 75–311). US Dept. of the Interior, Geological Survey, National Center for Earthquake Research. (1975).
82. Rebez, A. & Renner, G. Duration magnitude for the northeastern Italy seismometric network. *Boll di geof teo ed. appl.* **33**, 177–186 (1991).
83. Bragato, P. L. & Tento, A. Local magnitude in northeastern Italy. *Bull. Seismol. Soc. Am.* **95**, 579–591 (2005).
84. Lomax, A. The 2020 Mw 6.5 Monte Cristo Range, Nevada earthquake: relocated seismicity shows rupture of a complete shear-crack system. *EarthArXiv* https://doi.org/10.31223/X5X015 (2020).
85. Lomax, A., Virieux, J., Volant, P. & Berge-Thierry, C. Probabilistic earthquake location in 3D and layered models: Introduction of a Metropolis-Gibbs method and comparison with linear locations. In *Advances in seismic event location* (Springer Netherlands, 2000).
86. Lomax, A., Michelini, A. & Curtis, A. Earthquake location, direct, global-search methods. In *Encyclopedia of Complexity and Systems Science* (ed. Meyers, R. A.) (Springer New York, 2014). https://doi.org/10.1007/978-3-642-27737-5_150-2
87. De Landro, G. et al. 3D structure and dynamics of Campi Flegrei enhance multi-hazard assessment. *Nat. Commun.* **16**, 4814. https://doi.org/10.1038/s41467-025-59681-0 (2025).
88. Gentile, G. F., Bressan, G., Burlini, L. & De Franco, R. Three-dimensional Vp and Vp/Vs models of the upper crust in the Friuli area (northeastern Italy). *Geophys. J. Int.* **141**, 457–478 (2000).
89. Magrin, A. & Rossi, G. Deriving a new crustal model of Northern Adria: the Northern Adria Crust (NAC) model. *Front. Earth Sci.* **8**, 89 (2020).
90. Geller, R. J. & Mueller, C. S. Four similar earthquakes in central California. *Geophys. Res. Lett.* **7**, 821–824 (1980).
91. Nadeau, R., Antolik, M., Johnson, P. A., Foxall, W. & McEvilly, T. V. Seismological studies at Parkfield III: Microearthquake clusters in the study of fault-zone dynamics. *Bull. Seism Soc. Am.* **84**, 247–263 (1994).
92. Poupinet, G., Glangeaud, F. & Cote, P. P-Time delay measurement of a doublet of microearthquakes. In *ICASSP'82. IEEE International Conference on Acoustics, Speech, and Signal Processing*, Vol. 7, 1516–1519 (IEEE, 1982).
93. Poupinet, G., Ellsworth, W. L. & Fréchet, J. Monitoring velocity variations in the crust using earthquake doublets: An application to the Calaveras Fault, California. *J. Geoph Res. : Solid Earth*. **89**(B7), 5719–5731 (1984).
94. Delaunay, B. Sur la sphere vide (On the empty sphere). *Bull. de l'Académie des. Sci. de l'URSS Classe des. Sci. Mathématiques et Nat.* **6**, 793–800 (1934).
95. Halko, N., Martinsson, P. G. & Tropp, J. A. Finding structure with randomness: probabilistic algorithms for constructing approximate matrix decompositions. https://doi.org/10.1137/090771806, **53**(2), 217–288 (2011).
96. Romano, M. A. et al. Constraining tectonic structures at depth through seismicity revision and tomographic analysis: two case studies in the ESA (Eastern Southern Alps, Italy). In *Fault segmentation and seismotectonics of active thrust systems: the Northern Apennines and Southern Alps laboratories for new seismic hazard assessments (NASA4SHA). Selected outcomes and results from the PRIN2020 Project,* Vol. 102, 131–136 (2025).
97. Sugan, M. et al. Focal mechanisms of the southeastern Alps and surroundings (2.0) [Data set]. *Zenodo* https://doi.org/10.5281/zenodo.10853582 (2024).
98. Michelini, A. & Bolt, B. Application of the principal parameters method to the Coalinga, California, aftershock sequence. *Bull. Seis Soc. Am.* **76**, 409–420 (1986).
99. Rossi, G. & Ebblin, C. Space (3-D) and space-time (4-D) analysis of aftershock sequences: the Friuli (NE Italy) case. *Boll. Geof Teor Appl.* **22**, 37–49 (1990).

Acknowledgements

The authors gratefully acknowledge Giuliana Rossi for valuable discussions and Enrico Magrin for providing the computational resources used in this work.

Author contributions

PB and MP conceived and designed the study. GDL contributed to its conception. PB acquired the data and, together with MP, performed the data analysis. PB carried out the precise relocation analysis, MP conducted the cluster identification analysis, and AGI performed the PCA. All authors contributed to the interpretation of the results and to manuscript writing.

Funding

This work has been financially supported by the EPOS Research Infrastructure through the contribution of the Italian Ministry of University and Research (MUR)- EPOS ITALIA Joint Research Unit. This research was supported by the PRIN 2022 project '2022ZHXWC9'—Intercepting the PREparatory Phase of lARge earthquakes from seismic information and gEodetic Displacement (PREPARED)—and by the Interreg VI-A Italy-Slovenia project ITA-SI0800359—CONCORDIA.

Declarations

Competing interests

The authors declare no competing interests.

Additional information

Supplementary Information The online version contains supplementary material available at https://doi.org/10.1038/s41598-026-68819-6.

Correspondence and requests for materials should be addressed to P.B.

Reprints and permissions information is available at www.nature.com/reprints.

Publisher's note Springer Nature remains neutral with regard to jurisdictional claims in published maps and institutional affiliations.

Open Access This article is licensed under a Creative Commons Attribution 4.0 International License, which permits use, sharing, adaptation, distribution and reproduction in any medium or format, as long as you give appropriate credit to the original author(s) and the source, provide a link to the Creative Commons licence, and indicate if changes were made. The images or other third party material in this article are included in the article's Creative Commons licence, unless indicated otherwise in a credit line to the material. If material is not included in the article's Creative Commons licence and your intended use is not permitted by statutory regulation or exceeds the permitted use, you will need to obtain permission directly from the copyright holder. To view a copy of this licence, visit http://creativecommons.org/licenses/by/4.0/.

© The Author(s) 2026